Mass-loss along the red giant branch in 46 globular clusters and their multiple populations

M. Tailo [1]★ A. P. Milone [1,2] E. P. Lagioia [1,2] F. D'Antona,[3] A. F. Marino [1,2,4] E. Vesperini,[5] V. Caloi,[6] P. Ventura,[3] E. Dondoglio[1] and G. Cordoni [1]

[1]*Dipartimento di Fisica e Astronomia 'Galileo Galilei', Univ. di Padova, Vicolo dell'Osservatorio 3, I-35122 Padova, Italy*
[2]*Istituto Nazionale di Astrofisica – Osservatorio Astronomico di Padova, Vicolo dell'Osservatorio 5, I-35122 Padova, Italy*
[3]*Istituto Nazionale di Astrofisica – Osservatorio Astronomico di Roma, Via Frascati 33, I-00040 Monteporzio Catone, Roma, Italy*
[4]*Centro di Ateneo di Studi e Attivita' Spaziali 'Giuseppe Colombo' – CISAS, Via Venezia 15, I-35131 Padova, Italy*
[5]*Department of Astronomy, Indiana University, Bloomington, IN 47405, USA*
[6]*INAF – IASF Roma, Via Fosso del Cavaliere, I-00133 Roma, Italy*

ABSTRACT

The location of Galactic globular clusters' (GC) stars on the horizontal branch (HB) should mainly depend on GC metallicity, the 'first parameter', but it is actually the result of complex interactions between the red giant branch (RGB) mass-loss, the coexistence of multiple stellar populations with different helium content, and the presence of a 'second parameter' that produces dramatic differences in HB morphology of GCs of similar metallicity and ages (like the pair M3–M13). In this work, we combine the entire data set from the *Hubble Space Telescope* Treasury survey and stellar evolutionary models, to analyse the HBs of 46 GCs. For the first time in a large sample of GCs, we generate population synthesis models, where the helium abundances for the first and the 'extreme' second generations are constrained using independent measurements based on RGB stars. The main results are as follows: (1) The mass-loss of first-generation stars is tightly correlated to cluster metallicity. (2) The location of helium enriched stars on the HB is reproduced only by adopting a higher RGB mass-loss than for the first generation. The *difference* in mass-loss correlates with helium enhancement and cluster mass. (3) A model of 'pre-main sequence disc early loss', previously developed by the authors, explains such a mass-loss increase and is consistent with the findings of multiple-population formation models predicting that populations more enhanced in helium tend to form with higher stellar densities and concentrations. (4) Helium-enhancement and mass-loss both contribute to the second parameter.

Key words: stars: evolution – stars: fundamental parameters – stars: horizontal branch – stars: mass-loss – globular clusters: general.

1 INTRODUCTION

The study of the horizontal branch (HB), the locus of the colour–magnitude diagram (CMD) populated by stars burning helium in their core, is crucial to understand stellar evolution and characterize the stellar populations in globular clusters (GCs).

The HB stars are the direct off-springs of the red giant branch ones (RGB) and reach the helium burning stage after the ignition of their degenerate helium core in a process dubbed core-helium flash. The initial mass of the evolving stars (depending on the cluster age and metallicity – iron and light elements, mainly CNO, content) and the mass-loss on the RGB (subject to some cosmic spread) determine the final masses which populate the HB. Fixed the chemical composition, a larger RGB mass-loss is needed to reach a larger effective temperature ($T_{\rm eff}$) on the HB, as the HB mass decreases for increasing $T_{\rm eff}$. Increasing the metallicity, each mass moves to lower $T_{\rm eff}$ values, so the metallicity constitutes the 'first parameter' of the HB morphology (e.g. Arp, Baum & Sandage 1952).

Assuming that all the cluster stars have the same helium content, probably the abundance emerging from the big bang nucleosynthesis, it was soon clearly that the morphology of the HB could be widely different even in GCs with similar age and metallicity, and that a 'second parameter' was at play (see e.g. Sandage & Wildey 1967a; Fusi Pecci et al. 1993). A classical example is the pair NGC 5272 (M 3) and NGC 6205 (M 13), showing radically different HBs. A different mass-loss on the RGB was considered the main reason for the different HB morphology, but no clear association of this systemic mass-loss difference with other cluster physical parameters was conclusively found.

A major obstacle to understand the observed HB of GCs is that the parameters at play are often degenerate, so that a number of different combinations of age, metallicity, helium, and mass-loss provide similar HBs. In part, the parameter degeneracy is limited by adopting ages inferred from the main-sequence turn-off and metallicities obtained from spectroscopy.

The evidence that nearly all GCs host multiple stellar populations with different helium abundances has provided an additional challenge to explain their HBs. Indeed, helium enhanced stars evolve more rapidly than stars with $Y \sim 0.25$, thus, for fixed metallicity, age, and mass-loss in the RGB stage, they produce less massive

★ E-mail: mrctailo@gmail.com, marco.tailo@unipd.it

HB stars, which exhibit bluer colours (e.g. Iben & Renzini 1984; D'Antona et al. 2002; D'Antona & Caloi 2004). Thus, in single age, monometallic GCs, the second-generation stars (2G), usually helium enhanced, will exhibit bluer colours than the first-generation ones (1G). Nevertheless, it is difficult to disentangle between helium and mass-loss from the observed HBs, because increasing the helium content works in the same direction of increasing mass-loss (e.g. D'Antona et al. 2002). Without external constraints, the approach adopted in most HB studies, used in both classical and more recent works (such as D'Antona et al. 2002; D'Antona & Caloi 2004; D'Antona et al. 2005; Caloi & D'Antona 2008; di Criscienzo et al. 2010; Gratton et al. 2010; Dalessandro et al. 2011; D'Antona et al. 2013; Dalessandro et al. 2013; VandenBerg, Denissenkov & Catelan 2016; VandenBerg & Denissenkov 2018) is to estimate both helium abundance and mass-loss from the HB itself. Hence, the complete set of parameters for each group of stars on the HB is still degenerate.

A way to estimate the helium mass fraction in the 2G stars and break the parameters degeneracy on the HB is to use a theoretical scenario that describes the formation of multiple populations and predicts their helium contents. Recent examples are Tailo et al. (2016, 2017) and Jang, Kim & Lee (2019), who use the asymptotic giant branch (AGB) scenario (D'Ercole et al. 2008; Ventura & D'Antona 2010; D'Ercole et al. 2012, and references therein) and the scenario from Kim & Lee (2018, and references therein), respectively. The theoretical uncertainties on the nature of the polluter stars and the dynamical evolution of the populations, however, make this approach still uncertain (see Renzini et al. 2015, for a review).

Recent work proposed a new approach to disentangle between the effect of helium and mass-loss along the HB of GCs. Tailo et al. (2019a) studied M 4, which is one of the simplest GCs in the context of multiple populations. Indeed, it hosts two distinct groups of 1G and 2G stars that can be identified along the main evolutionary phases (Marino et al. 2008, 2017), including the MS and the HB. In particular, the red HB of M 4 is composed of 1G stars, whereas blue-HB stars belong to the 2G as inferred from high-resolution spectroscopy (Marino et al. 2011). Based on multiband *Hubble Space Telescope* (*HST*) photometry of MS stars, Tailo et al. (2019a) first obtained accurate determinations of the helium abundances of 1G and 2G stars. Then, they used their helium determinations to fix the helium content of stellar populations along the HB and constrain their mass-losses. Intriguingly, Tailo and collaborators find that 2G stars lose more mass than the 1G and similar conclusions come from a similar investigation on multiple populations in M 3 (Tailo et al. 2019b).

The fact that the helium abundances of multiple stellar populations are now available for more than 70 GCs (e.g. Lagioia et al. 2018, 2019; Milone et al. 2018, 2020; Zennaro et al. 2019, and references therein) allows to infer the mass-loss in a large sample of GCs.

In this work, we extend the method by Tailo et al. (2019a) to a large sample of 46 GCs to estimate, for the first time, the RGB mass-loss of their stellar populations. The paper is organized as follows. In Section 2, we present the observations and the theoretical models. Section 3 describes the procedure to infer the mass-loss of the distinct stellar populations in GCs. Results are presented in Section 4 and discussed in Section 5. Summary and conclusions follow in Section 6.

2 DATA AND MODELS

To derive the mass-loss of GCs, we combine multiband photometry from the *HST* UV legacy survey of GCs (Piotto et al. 2015), helium abundances of multiple populations from Milone et al. (2018), and stellar models suitable for GC stars with different helium content (Tailo 2016, and references therein). Sections 2.1, 2.2, and 2.3

describe the photometry, the helium abundances, and the theoretical models, respectively.

2.1 Photometric data set

To analyse the HBs of GCs, we exploited the photometric and astrometric catalogues from the *HST* UV legacy survey of GCs (Piotto et al. 2015; Nardiello et al. 2018), which include astrometry and photometry in the *F275W*, *F336W*, *F438W* photometric bands of the ultraviolet and visual channel of the wide-field camera 3 and in the *F606W* and *F814W* bands of the Wide Field Channel of the Advanced Camera for Surveys. We refer to Piotto et al. (2015) and Nardiello et al. (2018) for details on the data set and on the data reduction. Photometry has been corrected for differential reddening as in Milone et al. (2012a).

2.2 Helium abundances of multiple populations

The helium abundances adopted in this study are provided by Milone et al. (2018). These authors used multiband *HST* photometry to analyse the groups of 1G and 2G stars and the group of 2G stars with extreme chemical composition (2Ge) identified by Milone et al. (2017) based on the pseudo two-colour diagram called chromosome map (Milone et al. 2015). They provide the average helium contents of 2G and 2Ge stars, relative to the helium abundance of 1G stars ($\delta Y_{2G,1G}$ and δY_{max}). We point out that while in our previous studies and in the literature the term 'extreme 2G population' often refers to those stars with very high helium abundances present only in some clusters, here the 2Ge is defined for each cluster as *the most extreme 2G population within that cluster*.

2.3 Stellar models

We adopted the stellar-evolution models and the isochrones used by Tailo et al. (2016, 2017, 2019a, b), which are obtained with the stellar-evolution program ATON 2.0 by Ventura et al. (1998) and Mazzitelli, D'Antona & Ventura (1999). We calculated a grid of models with different ages, metallicities (Z), and helium mass fractions (Y). In particular, our models range from [Fe/H] = -2.44 to -0.45 and from $Y = 0.25$ to 0.40, thus accounting for the metallicity and helium enhancement values of all studied GCs. The helium mass fraction of the HB models includes the small correction due to the effect of the first dredge up. The HB evolution is followed until the end of the helium burning phase using the recipes of D'Antona et al. (2002).

We compared the m_{F438W} versus $m_{F438W} - m_{F814W}$ CMD of the observed HB of each clusters with a grid of synthetic CMDs derived from the corresponding models following the recipes of D'Antona et al. (2005, and references therein). In a nutshell, we determine the mass of the each HB star (M^{HB}) in the simulations as follows: $M^{HB} = M^{Tip}(\mathbf{Z}, Y, A) - \Delta M(\mu, \delta)$. Here, M^{Tip} is the stellar mass at the RGB tip, and depends on age (A), metallicity (Z), and helium content (Y); ΔM is the mass lost by the star, which is described by a Gaussian profile with central value μ and standard deviation δ. The values of M^{Tip} are obtained from the isochrones data base. Once the mass of an HB star has been determined, the programme locates it on the models grid via a series of interpolations. The HB age of a star is then extracted from a uniform random distribution ranging from the zero age HB locus (ZAHB) to the end of the core helium burning phase. The uneven distribution with time of the points along the tracks ensures that the evolution speed information is preserved. We simulate the effect of radiative levitation of metals in stars with effective temperatures between 11 500 and 18 000 K by increasing

their atmospheric metal content to super solar values (equivalent to [Fe/H] = 0.2) as suggested by Brown et al. (2016, and references therein) and Tailo et al. (2017, and references therein). This process reproduces the effects of the Grundahl et al. (1999) jump.

3 DERIVING THE MASS-LOSS OF MULTIPLE POPULATIONS

To infer the mass-loss of stellar populations, we exploit the procedure introduced by Tailo et al. (2019a, b), which is based on the hypothesis that 1G stars mostly populate the reddest part of the HB in CMDs made with optical filter, whereas the 2Ge stars are located on the hottest HB side. As discussed in the introduction, such hypothesis, true for the Type I clusters (as defined in Milone et al. 2017), is supported both by theoretical arguments (e.g. D'Antona et al. 2002; Caloi & D'Antona 2008) and by direct spectroscopic studies of 1G and 2G stars along the HB (e.g. Marino et al. 2011, 2014).

By limiting the analysis to the easily defined groups at the lowest and highest $T_{\rm eff}$'s of the HB, we avoid in this work the more ambiguous identification and analysis of the intermediate populations, which require an extensive and non homogeneous cluster-by-cluster consideration.

Metal-rich GCs, with an only-red HB provide remarkable exceptions. Indeed, their 1G and 2G HB stars are partially mixed in optical CMDs and appropriate two-colour diagrams are needed to identify multiple populations along the HB (Milone et al. 2012b).

In the following, we describe the procedures used to investigate multiple populations in GCs with an HB extending to the blue, and in metal-rich GCs with an only-red HB, by exploiting the recipes by Tailo et al. (2019a, b). The main quantities characterizing HB stars and estimated in this work include mass-loss of 1G stars (μ_{1G}), mass-loss of 2G stars (μ_{2G}) and of 2G stars with extreme chemical composition (2Ge, μ_{2Ge}). We will also derive the average HB masses of 1G, 2G, and 2Ge stars ($\bar{M}_{1G}^{HB}$, $\bar{M}_{2G}^{HB}$, and $\bar{M}_{2Ge}^{HB}$) and the difference between the mass-loss of 2Ge and 1G stars, $\Delta\mu_e$. To do this, we consider as test cases two clusters with very different HB morphologies: NGC 6752, which exhibits an extended HB and is representative of the majority of the studied GCs, and NGC 6637, which has an only–red HB.

3.1 Clusters with blue HB: NGC 6752

3.1.1 Mass-loss of first-generation stars

To derive the mass-loss of 1G stars in NGC 6752, we generate simulated HB CMDs based on a grid of HB tracks for 1G. The tracks have the helium core mass at which the RGB evolution ignites the helium flash, and different masses in the hydrogen envelopes, standard helium abundance ($Y = 0.25$) and the cluster metallicity.

Each simulation adopts the parameters inferred from the best-fitting isochrone[1] for the RGB mass, the mass lost during the RGB evolution (μ_{1G}) and a mass-loss spread (δ). A large grid of

---

[1]The isochrone that provides the best fit with the observed CMD is derived as in previous papers from our group (e.g. Tailo et al. 2019b). In a nutshell, we assumed $Y = 0.25$, $[\alpha/\text{Fe}] = +0.4$ and adopted the value of [Fe/H], distance modulus and reddening provided by the 2010 version of the Harris (1996) catalogue. We produced a set of appropriate isochrones with ages between 10.0 and 14.5 Gyr in steps of 0.25 Gyr. The best age determination is given by the isochrone that provides the best match with the region of the $m_{F438W} - m_{F606W}$ versus m_{F606W} CMD around the MS turn-off, the corresponding uncertainty corresponds to the range of ages that allow the

simulations is built, by varying μ_{1G} from 0.100 to 0.310 M$_\odot$ in steps of 0.003 M$_\odot$ and δ from 0.002 to 0.008 M$_\odot$ in steps of 0.001 M$_\odot$.

The normalized histogram colour distribution of each simulation is compared with the corresponding colour distribution of candidate 1G stars of NGC 6752, by means of the χ-square distance (hereinafter χ_d^2, see e.g. Dodge 2008):

$$\chi_d^2 = 0.5 \times \sum_i \frac{(p_i - q_i)^2}{(p_i + q_i)},$$

where p_i and q_i are the values of each bin of the observed and simulated histogram, respectively. Candidate 1G stars include the observed HB stars redder than $\overline{\text{col}}_{\rm sim} - 1.5 \times \sigma_{\rm col,sim}$, where $\overline{\text{col}}_{\rm sim}$ is the average $m_{F438W} - m_{F814W}$ colour of simulated stars and $\sigma_{\rm col,sim}$ is the corresponding standard deviation.

To qualitatively discuss the effect of changing mass-loss on the simulation, we note that, as the adopted value of μ_{1G} increases (decreases), simulated HB stars with fixed mass-loss spread move towards bluer (redder) average colours. Hence, the blue boundary of the observed 1G candidates is also blue-(red-) shifted and the comparison between the distributions of simulated and observed histograms would involve progressively bluer (redder) observed stars. As a consequence, too-high values of μ_{1G} would result into simulated HBs that are bluer than the bulk of observed 1G stars. On the other side, too-small values of μ_{1G} would provide HB stars that are redder than all observed HB stars. Both situations would provide high χ_d^2 values.

In a similar way, as δ increases (decreases) the simulations span a wider (narrower) range of M^{HB} values thus covering a larger (smaller) portion of the theoretical HB. The value of $\sigma_{\rm col,sim}$ increases (diminishes) accordingly and so does the portion of observed HB that the simulation covers. If we are using a value of δ too high (low), stars also belonging to the 2G might be included in the comparison (or stars belonging to the 1G might be excluded).

The best estimates of mass-loss and mass-loss spread for 1G stars are given by the values of μ_{1G} and δ of the simulations that provide the minimum χ_d^2. Uncertainties are estimated by means of bootstrapping. Specifically, we generated 5000 realizations of the HB in NGC 6752 and estimated μ_{1G} and δ by using the procedure described above. The uncertainties correspond to the standard deviations of the 5000 values of μ_{1G} and δ. We obtain for NGC 6752 $\mu_{1G} = 0.216 \pm 0.007$ and $\delta = 0.006 \pm 0.001$ M$_\odot$.

We derived the average mass of 1G stars along the HB ($\bar{M}_{1G}^{HB}$) by subtracting from the mass of 1G stars at the RGB tip provided by the best-fitting isochrone, $M_{1G}^{Tip} = 0.814$ M$_\odot$, the average mass-loss of the 1G. We find $\bar{M}_{1G}^{HB} = 0.598 \pm 0.007$ M$_\odot$ for NGC 6752.

Results are listed in Table 2 and illustrated in Fig. 1, where we compare the observed m_{F814W} versus $m_{F438W} - m_{F814W}$ CMD of HB stars in NGC 6752 with the contours of the best-fitting simulated 1G (panel a). For completeness, we also show the normalized histogram distribution of the colours of HB stars (Fig. 1b) and the comparison between the normalized histogram distributions of simulated stars and the candidate 1G stars (Fig. 1c, which includes HB stars redder than the vertical dashed line plotted in panel b). Finally, we show in Fig. 1(d) the χ_d^2 map in the μ_{1G}–δ plane, where the orange square marks the best determinations of μ_{1G} and δ.

As a sanity check, we have verified that the reddest group of stars has been correctly identified by also comparing the simulation with the data in the $m_{F275W} - m_{F814W}$ versus m_{F275W} CMD (see Fig. 2).

---

isochrones to envelope 68.27 per cent of the turn-off stars. We derive for NGC 6752 an age of 13.00 ± 0.50 Gyr.
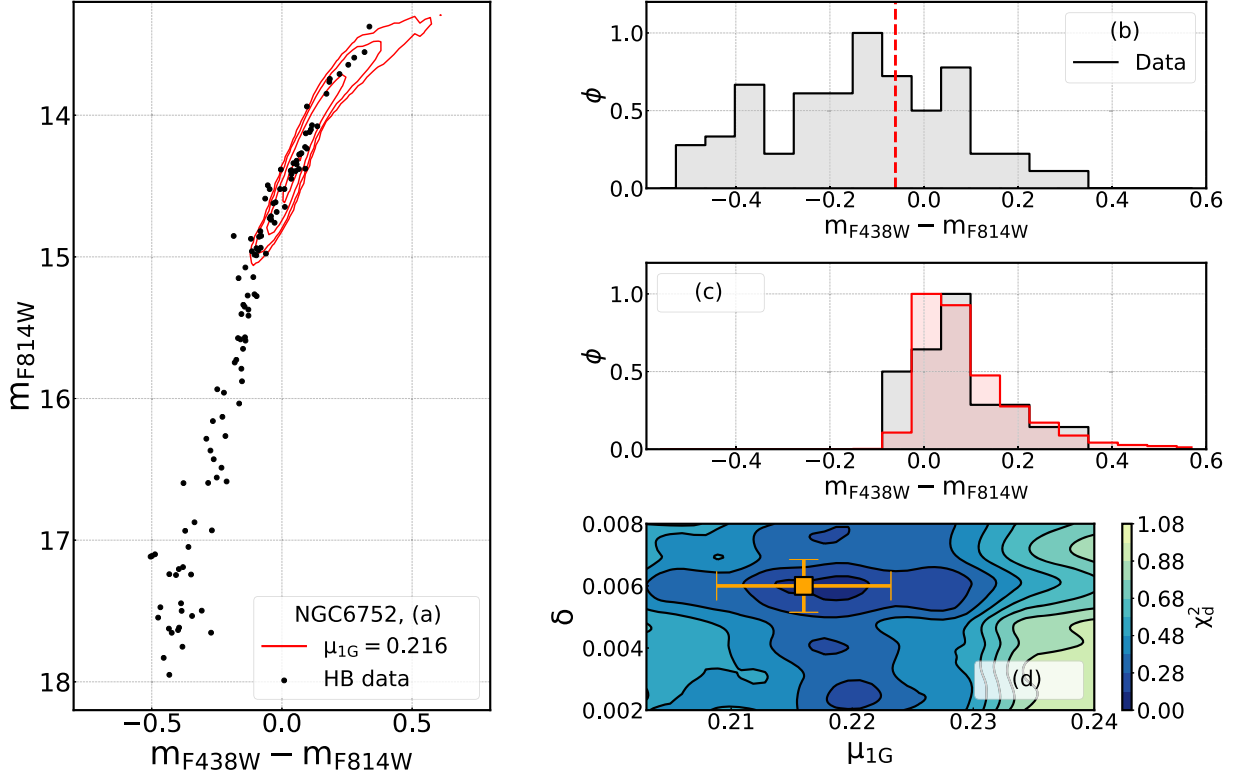
Figure 1. This figure illustrates the procedure to infer the mass-loss of 1G stars in NGC 6752. Panel a compares the observed CMD of HB stars (black dots) with the contours of the simulated 1G that provides the best match with the observation. The normalized histogram distribution of all HB stars is plotted in panel b, while panel c compares the histogram of simulated 1G stars (red histogram) with the histogram of the observed candidate 1G stars (grey histogram), which comprise HB stars with redder $m_{F438W}-m_{F814W}$ colours than the vertical dashed line plotted in panel b. Panel d shows the map of χ_d^2 in the δ versus μ_{1G} plane. The best determination of mass-loss and mass-loss spread are indicated by the orange square, while the error bars indicate the uncertainties derived by means of bootstrapping (see text for details).
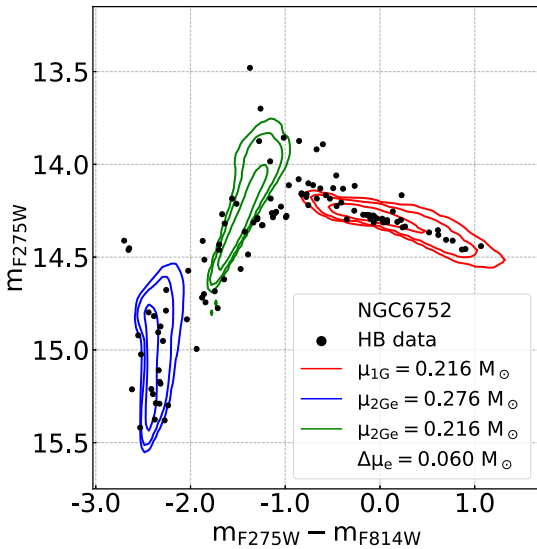

Figure 2. The $m_{F275W}-m_{F814W}$ versus m_{F275W} CMD for NGC 6752 where we overplot our best-fitting simulations as contour plots, with red and blue respectively for the 1G and the 2Ge. The green contour plot represents the 2Ge simulation but with the same mass-loss value of the 1G, as indicated in the label.

3.1.2 Mass-loss of extreme second-generation stars

The procedure to infer the mass-loss of 2Ge stars is similar to the method described in the previous section for the 1G, but is based on the assumption that 2Ge stars populate the bluest, faintest tail of the HB.

We generate a grid of simulated HBs of 2Ge stars by assuming the same parameters (age, metallicity, mass-loss, and mass-loss spread) used for the 1G but different helium content. Specifically, the value of Y in the HB tracks is increased by the amount inferred by Milone et al. ([2018](#)) for the extreme population, which is $Y = 0.292$ for NGC 6752. This same helium abundance is used to infer the 2Ge mass evolving on the RGB at the cluster age of 13 Gyr. The normalized histogram distribution in m_{F814W} of each simulation is compared with the corresponding magnitude distribution of the observed candidate 2Ge HB stars, by means of the χ-square distance. Candidate 2Ge stars include HB stars fainter than $\overline{mag}_{sim} - 1.5 \times \sigma_{mag,sim}$, where $\overline{mag}_{sim}$ and $\sigma_{mag,sim}$ are the mean and standard deviation of the $F814W$ magnitudes of observed HB stars.

As the value of μ_{2Ge} increases (decreases), $\overline{mag}_{sim}$ and the whole simulation move towards higher (lower) magnitudes, describing a bunch of progressively fainter (brighter) stars. On the other hand, if the value of δ increases (decreases) the simulations overlap larger (smaller) sections of the HB. Considerations similar to those of the 1G case hold here, thus the value of χ_d^2 increases as the agreement between the two histograms worsens. The best estimates of the mass-loss of 2Ge stars μ_{2Ge} and δ for 2Ge stars are derived by means of
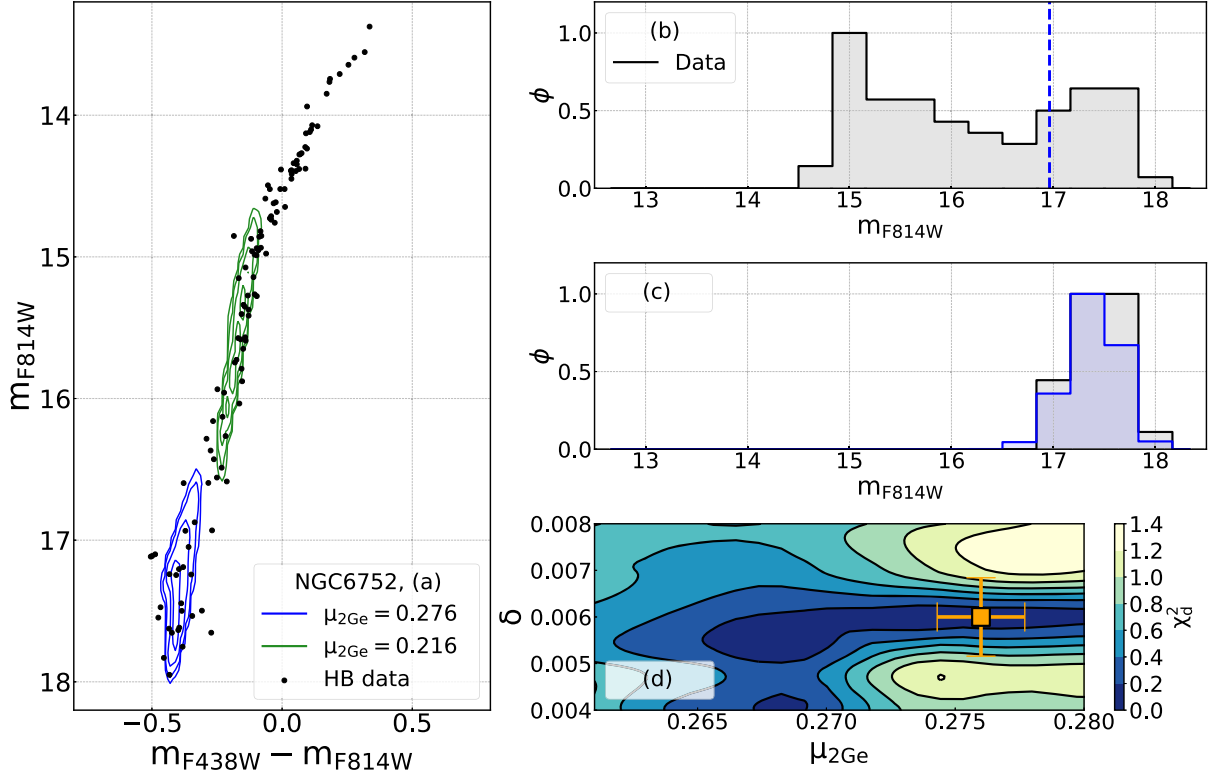
Figure 3. Procedure to derive the mass-loss of 2Ge HB stars. Panels a and b show the observed CMD of all HB stars (black points) and the histogram distributions of the *F814W* magnitude, respectively. The black histogram plotted in panel c shows the magnitude distributions of candidate 2Ge stars (i.e. stars fainter than the vertical dashed line plotted in panel b) and is compared with the distribution of the best-fitting simulated HB 2Ge stars (blue histogram). The blue contours shown in the panel a CMD correspond the best-fitting simulation of 2Ge stars, while the green contours correspond to a simulation with the same mass-loss as 1G stars. The map of χ_d^2 in the δ versus μ_{1G} plane is plotted in panel d, where the orange square mark the best determination of mass-loss and mass-loss spread. Error bars indicate the uncertainties obtained from bootstrapping (see text for details).

χ_d^2 minimization and the corresponding uncertainties are estimated by means of bootstrapping, in close analogy with what we did for the 1G. We find for 2Ge stars of NGC 6752 $\mu_{2Ge} = 0.276 \pm 0.002$ and $\delta = 0.006 \pm 0.001\,M_\odot$.

The comparison between the observed CMD of NGC 6752 (black dots) and the simulated CMD of 2Ge stars that provides the best fit (blue contours) is shown in Fig. 3(a). The result thus requires a 2Ge mass-loss larger by $\mu_{2Ge} - \mu_{1G} = 0.060\,M_\odot$ than the 1G mass-loss. In fact, if we simulate the CMD of 2Ge stars by assuming for both generations the mass-loss value inferred from 1G stars ($\mu_{2Ge} = \mu_{1G} = 0.216\,M_\odot$), the 2Ge group does not reproduce correctly the location of the extreme HB stars in NGC 6752 (green contours in Fig. 3a). Consequently, we conclude that the 2Ge stars of NGC 6752 lose more mass than the 1G.

The average mass of the 2Ge HB stars is the mass at the RGB tip $M_{2Ge}^{Tip} = 0.756\,M_\odot$, derived by the best-fitting isochrone with $Y = 0.292$, minus the best-fitting mass lost $\mu_{2Ge} = 0.276\,M_\odot$, that is $\bar{M}_{2Ge}^{HB} = 0.480 \pm 0.002\,M_\odot$.

To illustrate the main steps towards determining the mass-loss of 2Ge stars, we also show in Fig. 3 the histogram distribution of m_{F814W} for HB stars (panel b), the comparison between the histograms of candidate 2Ge stars and the best-fitting simulation (panel c) and the χ_d^2 map contour map in the δ versus μ_{2Ge} plane (panel d). As a sanity check, we verify that the algorithm has correctly identified the extreme HB stars by comparing the simulation with the data in the $m_{F275W} - m_{F814W}$ versus m_{F275W} CMD (see Fig. 2). Finally, in Figs 2 and 3(a) we show, for completeness, the simulation of the 2Ge HB stars obtained

with the same mass-loss we found for the 1G (thus $\mu_{2Ge} = \mu_{1G} = 0.216\,M_\odot$). This is clearly a bad simulation of the 2Ge, as the green curves do not reach the faintest part of the locus.

3.1.3 Impact of age, metallicity, and helium uncertainties on mass-loss

To quantify the impact of the uncertainties of age, metallicity, and helium abundances (hereafter σ_A, σ_{Fe}, and σ_Y) on mass-loss determinations, we followed the recipe by Tailo et al. (2019a). For simplicity, we assumed $\delta = 0.006\,M_\odot$.

To investigate the effect of age uncertainties, we repeated the procedures described in Sections 3.1.1 and 3.1.2 to derive the mass-losses of 1G and 2Ge stars by adopting ages that differ from the best-fitting age by $\pm\sigma_A$ (i.e. 12.50 and 13.50 Gyr for NGC 6752). We find that a change in age by ± 0.50 Gyr corresponds to a variation of $\mp 0.013\,M_\odot$ in both μ_{1G} and μ_{2Ge}. Hence, age uncertainties provide negligible effect on the difference between the mass-loss of 1G and 1G stars ($\Delta\mu_e$).

Similarly, to account for [Fe/H] uncertainties, we estimated the mass-losses of 1G and 2Ge stars by assuming iron abundances that differ from the value provided by Harris (1996) by $\pm\sigma_{Fe}$. A difference of ± 0.1 dex, which is the typical error on [Fe/H] inferred from spectroscopy, affects μ_{1G} and μ_{2Ge} by 0.017 and 0.010 $M_\odot$, respectively. Hence, the adopted uncertainty on iron abundance have a small impact on $\Delta\mu_e$ by 0.007 $M_\odot$.
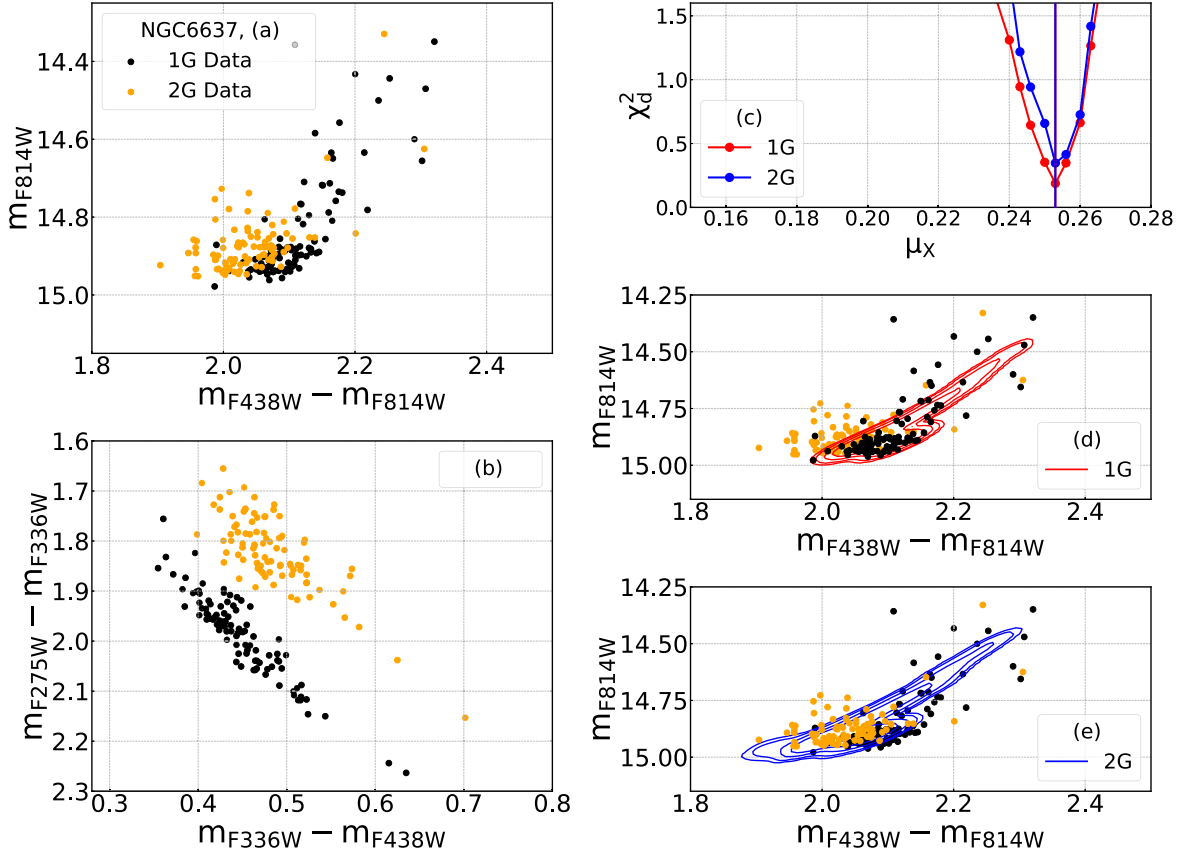
Figure 4. Procedure to derive the mass-loss of 1G and 2G stars of NGC 6637. Panels a and b show the m_{F814W} versus $m_{F438W} - m_{F814W}$ CMD and the $m_{F275W} - m_{F336W}$ versus $m_{F336W} - m_{F438W}$ two-colour diagram of HB stars. Panel c shows the χ_d^2 profiles for the mass-loss of 1G (red) and 2G stars (blue), while in panels d and e we superimpose on the observed CMD the contours of 1G and 2G stars that correspond to the best-fitting simulations. Observed 1G and 2G stars selected in the two-colour diagram of panel b are coloured black and yellow, respectively.

Finally, we considered the impact of helium uncertainties on mass-loss by changing the helium abundance of 2Ge stars by $\pm\sigma_Y$. We find that an helium variation of ± 0.004, as inferred by Milone et al. (2018) for 2Ge stars of NGC 6752, corresponds to a mass-loss change of $\mp 0.007\,\mathrm{M}_\odot$ on both μ_{2Ge} and $\Delta\mu_e$.

We conclude that, by combining in quadrature the effects of age, iron abundance, and helium content uncertainties, together with the one obtained from the bootstrapping procedure, our best estimate of the mass-loss in 1G stars is $\mu_{1G} = 0.216 \pm 0.022$, the estimate of mass-loss in 2Ge stars $\mu_{2Ge} = 0.276 \pm 0.023$ and, finally, the mass-loss difference in NGC 6752 is $\Delta\mu_e = 0.060 \pm 0.017\,\mathrm{M}_\odot$.

3.2 Clusters with no blue HB: the case of NGC 6637

1G and 2G stars of metal-rich GCs with only-red HB are mostly mixed in CMDs made with optical filters as illustrated in Fig. 4(a) for NGC 6637. Hence, we exploited the $m_{F275W} - m_{F336W}$ versus $m_{F336W} - m_{F438W}$ diagram, where 1G and 2G stars define distinct sequences, to identify multiple populations along the red HB (Milone et al. 2012b, see Fig. 4b for NGC 6637). Since this two-colour diagram does not provide clear separation among 2Ge stars and the remaining 2G stars, we limit the investigation to the entire sample of 2G stars.

To estimate the mass-loss of both 1G and 2G stars in GCs with the red HB alone, we used the procedure adopted for 1G stars of NGC 6752 (see Section 3.1.1), thus analysing the $m_{F438W} - m_{F814W}$

colour distribution of the HB stars. This is necessary because, when the HB stars are all on the red side, a large number of simulations occupy the same magnitude level. An additional remarkable difference is that we adopted the helium abundance of 2G stars inferred by Milone et al. (2018).

Results are summarized in the right panels of Fig. 4. We show the χ-square (see equation 1) resulting from the simulations with $\delta = 0.003$, corresponding to the position of the minima, against the mass-loss of 1G and 2G stars (panel c), and compare the contours of the simulations of 1G and 2G stars that correspond to the minimum χ_d^2 with the observed CMDs (panels c and d). Noticeably, both 1G and 2G stars of the HB in NGC 6637 are described by assuming the same mass-loss $\mu_{1G} = \mu_{2G} \sim 0.253\,\mathrm{M}_\odot$. The uncertainties on these values are evaluated with the procedure in Section 3.1.3 and are reported in Table 2.

4 RESULTS

The procedure described in the previous section for NGC 6752 has been extended to 34 GCs with blue HB. The parameters used as input for the simulations are listed in Table 1, while the resulting RGB-tip masses, mass-losses, and average HB masses of 1G and 2Ge stars are listed in upper part of Table 2, where we also provide the average mass-loss difference between 1G and 2Ge stars. For completeness, we included the results for NGC 5272 and NGC 6121 from Tailo et al. (2019a, b).

Table 1. Main GC parameters used in this work. For each cluster we provide: ID, average reddening, $E(B - V)$, distance module $[(m - M)_V]$ and [Fe/H] (from the 2010 version of the Harris 1996, catalogue), cluster ages (this work), helium difference between 2G and 1G stars ($\Delta Y_{2G,1G}$), and maximum helium abundance variation (from Milone et al. 2018) and GC group (adapted from Milone et al. 2014, see Section 4.1).

Cluster names	$E(B - V)$ (mag)	$(m - M)_V$ (mag)	[Fe/H]	[α/Fe]	Age (Gyr)	$\delta Y_{2G,1G}$	δY_{max}	Group
NGC 0104, 47 Tuc	0.04	13.37	−0.72	0.4	13.00 ± 0.75	0.011 ± 0.005	0.049 ± 0.005	M3-like
NGC 0288	0.03	14.84	−1.32	0.4	12.75 ± 0.50	0.015 ± 0.010	0.016 ± 0.012	M13-like
NGC 2298	0.14	15.60	−1.92	0.4	13.25 ± 0.50	−0.003 ± 0.008	0.011 ± 0.012	M13-like
NGC 2808	0.22	15.59	−1.14	0.4	12.00 ± 0.75	0.048 ± 0.005	0.124 ± 0.007	M3-like
NGC 3201	0.24	14.20	−1.59	0.4	12.00 ± 0.50	−0.001 ± 0.013	0.028 ± 0.032	M3-like
NGC 4590, M 68	0.05	15.21	−2.23	0.4	12.75 ± 0.75	0.007 ± 0.009	0.012 ± 0.009	M3-like
NGC 4833	0.32	15.08	−1.85	0.4	13.25 ± 0.50	0.016 ± 0.008	0.051 ± 0.009	M3-like
NGC 5024, M 53	0.02	16.32	−2.10	0.4	13.25 ± 0.75	0.013 ± 0.007	0.044 ± 0.008	M3-like
NGC 5053	0.01	16.23	−2.27	0.4	13.00 ± 0.50	−0.002 ± 0.013	0.004 ± 0.025	M3-like
NGC 5466	0.00	16.02	−1.98	0.4	12.75 ± 0.50	0.002 ± 0.013	0.007 ± 0.024	M3-like
NGC 5904, M 5	0.03	14.46	−1.29	0.4	12.25 ± 0.75	0.012 ± 0.004	0.037 ± 0.007	M3-like
NGC 5927	0.45	15.82	−0.49	0.2	12.25 ± 0.50	0.011 ± 0.004	0.055 ± 0.015	M3-like
NGC 5986	0.28	15.96	−1.59	0.4	13.25 ± 0.50	0.005 ± 0.006	0.031 ± 0.012	M13-like
NGC 6093, M 80	0.18	15.56	−1.75	0.4	13.50 ± 0.75	0.011 ± 0.008	0.027 ± 0.012	M13-like
NGC 6101	0.05	16.10	−1.98	0.4	12.75 ± 0.50	0.005 ± 0.010	0.017 ± 0.011	M13-like
NGC 6144	0.36	15.86	−1.76	0.4	13.00 ± 0.50	0.009 ± 0.011	0.017 ± 0.013	M13-like
NGC 6171, M 107	0.33	15.05	−1.00	0.4	12.50 ± 0.25	0.019 ± 0.011	0.024 ± 0.014	M3-like
NGC 6205, M 13	0.02	14.33	−1.52	0.4	12.25 ± 0.75	0.020 ± 0.004	0.052 ± 0.004	M13-like
NGC 6218, M 12	0.19	14.01	−1.37	0.4	13.00 ± 0.50	0.009 ± 0.007	0.011 ± 0.011	M13-like
NGC 6254, M 10	0.28	14.08	−1.56	0.4	12.75 ± 0.50	0.006 ± 0.008	0.029 ± 0.011	M13-like
NGC 6304	0.54	15.52	−0.45	0.2	12.50 ± 0.50	0.008 ± 0.005	0.025 ± 0.006	M3-like
NGC 6341, M 92	0.02	14.65	−2.31	0.4	13.50 ± 0.75	0.022 ± 0.004	0.039 ± 0.006	M3-like
NGC 6352	0.22	14.43	−0.64	0.2	12.75 ± 0.25	0.019 ± 0.014	0.027 ± 0.006	M3-like
NGC 6362	0.09	14.68	−1.00	0.4	12.25 ± 0.50	0.004 ± 0.011	0.004 ± 0.011	M3-like
NGC 6366	0.71	14.94	−0.59	0.2	12.25 ± 0.50	0.011 ± 0.010	0.011 ± 0.015	M3-like
NGC 6397	0.18	12.37	−2.00	0.4	13.00 ± 0.50	0.006 ± 0.009	0.008 ± 0.011	M13-like
NGC 6441	0.47	16.78	−0.46	0.2	12.25 ± 0.75	0.029 ± 0.006	0.081 ± 0.022	M3-like
NGC 6496	0.15	15.74	−0.46	0.2	12.00 ± 0.50	0.009 ± 0.011	0.021 ± 0.006	M3-like
NGC 6535	0.34	15.34	−1.79	0.4	13.25 ± 0.50	0.003 ± 0.021	0.003 ± 0.022	M13-like
NGC 6541	0.14	14.82	−1.81	0.4	13.00 ± 0.50	0.024 ± 0.005	0.045 ± 0.006	M13-like
NGC 6584	0.10	15.96	−1.50	0.4	12.25 ± 0.75	0.000 ± 0.007	0.015 ± 0.011	M3-like
NGC 6624	0.28	15.36	−0.44	0.2	12.50 ± 0.50	0.010 ± 0.004	0.022 ± 0.003	M3-like
NGC 6637	0.18	15.28	−0.64	0.2	12.25 ± 0.50	0.004 ± 0.006	0.011 ± 0.005	M3-like
NGC 6652	0.09	15.28	−0.81	0.4	13.25 ± 0.25	0.008 ± 0.007	0.017 ± 0.011	M3-like
NGC 6681, M 70	0.07	14.99	−1.62	0.4	13.25 ± 0.75	0.009 ± 0.008	0.029 ± 0.015	M13-like
NGC 6717, Pal 9	0.22	14.94	−1.28	0.4	13.00 ± 0.25	0.003 ± 0.006	0.003 ± 0.009	M13-like
NGC 6723	0.05	14.84	−1.10	0.4	13.00 ± 0.75	0.005 ± 0.006	0.024 ± 0.007	M3-like
NGC 6752	0.04	13.13	−1.54	0.4	13.00 ± 0.50	0.015 ± 0.005	0.042 ± 0.004	M13-like
NGC 6779, M 56	0.26	15.68	−1.99	0.4	13.50 ± 0.50	0.011 ± 0.007	0.031 ± 0.008	M13-like
NGC 6809, M 55	0.08	13.89	−1.94	0.4	13.25 ± 0.50	0.014 ± 0.008	0.026 ± 0.015	M13-like
NGC 6838, M 71	0.25	13.80	−0.78	0.4	12.75 ± 0.50	0.005 ± 0.009	0.024 ± 0.010	M3-like
NGC 6981, M 72	0.05	16.31	−1.42	0.4	12.25 ± 0.75	0.011 ± 0.006	0.017 ± 0.006	M3-like
NGC 7078, M 15	0.10	15.39	−2.37	0.4	13.00 ± 0.75	0.021 ± 0.009	0.069 ± 0.006	M3-like
NGC 7099, M 30	0.03	14.64	−2.27	0.4	13.50 ± 0.50	0.015 ± 0.010	0.022 ± 0.010	M13-like

The input parameters adopted for 10 GCs with red-only HB, and the resulting RGB-tip masses, mass-losses, average masses of 1G and 2G stars, and mass-loss difference between 1G and 2G stars are listed in Table 1 and in the lower part of Table 2, respectively.

We conducted a series of tests to ensure that our results are not affected by the most common biases of this kind of analysis. (A) We verified that the results for our GC sample are not dependent on the exact binning choices. We tested a few sample cases halving the binning step and verified that the values we get are compatible. (B) We verified that our results are not biased by the exact metric normalization by re-examining a few cases changing the normalization criterion of the simulation histograms; specifically, we repeated the comparison normalizing the simulation histogram to the same number of stars in the target populations and verified that

the results obtained with the two methods are compatible. (C) We verified that the identifications provided by our searching algorithm are compatible with the ones obtained from independent sources (e.g. in the case of 6441 by comparing our identification with the one provided via a colour–colour diagram similar to the one in Fig. 4. (D) We verified that our algorithm is capable of recovering the parameters of the target populations from a toy HB model, where we know exactly the input parameters of the 1G and 2Ge stars. (E) We look at our results in the $m_{F275W} - m_{F814W}$ versus m_{F275W} CMD, similar to the one in Fig. 2, as a sanity check for the population identification.

The complete showcase of the HBs analysed in this work is provided in Appendix A, where we compare the CMDs our GCs with the contours of the simulated CMDs that provide the best match with the observed 1G and 2Ge HB stars.

Table 2. This table lists the main quantities derived in this paper, including stellar mass at the RGB tip (M^{Tip}), mass-loss (μ), average mass on HB stars (M^{HB}) for 1G, 2Ge, and 2G stars. We also provide the values of the Reimers' parameter η_R inferred for each cluster, the mass-loss difference between 2Ge and 1G stars ($\Delta\mu_e$) and the internal mass-loss spread (δ). We point out that, although evaluated independently, we obtain equal values of δ for both the 1G and the 2Ge in all the examined GCs. We therefore report a single value for this quantity in the table. The error values of these quantities, where appropriate, are obtained from the combination in quadrature of all different sources (see text). (a) From Tailo et al. (2019b), (b) from Tailo et al. (2019a).

ID	M^{Tip}_{1G} (M$_\odot$)	μ_{1G} (M$_\odot$)	$\bar{M}^{\text{HB}}_{1G}$ (M$_\odot$)	$\eta_{R,1G}$	M^{Tip}_{2Ge} (M$_\odot$)	μ_{2Ge} (M$_\odot$)	$\bar{M}^{\text{HB}}_{2Ge}$ (M$_\odot$)	$\Delta\mu_e$ (M$_\odot$)	δ (M$_\odot$)
NGC 0288	0.817	0.213 ± 0.021	0.604 ± 0.021	0.516 ± 0.021	0.795	0.246 ± 0.025	0.546 ± 0.025	0.033 ± 0.020	0.004 ± 0.001
NGC 2298	0.789	0.116 ± 0.015	0.676 ± 0.015	0.278 ± 0.020	0.775	0.156 ± 0.023	0.619 ± 0.023	0.040 ± 0.023	0.004 ± 0.001
NGC 2808	0.828	0.113 ± 0.024	0.715 ± 0.024	0.242 ± 0.032	0.661	0.216 ± 0.025	0.445 ± 0.025	0.103 ± 0.012	0.005 ± 0.001
NGC 3201	0.821	0.116 ± 0.024	0.705 ± 0.024	0.270 ± 0.033	0.782	0.139 ± 0.044	0.642 ± 0.044	0.023 ± 0.042	0.005 ± 0.001
NGC 4590, M 68	0.794	0.043 ± 0.020	0.751 ± 0.020	0.120 ± 0.027	0.778	0.063 ± 0.020	0.715 ± 0.020	0.020 ± 0.026	0.006 ± 0.001
NGC 4833	0.791	0.123 ± 0.016	0.668 ± 0.016	0.306 ± 0.022	0.724	0.193 ± 0.022	0.531 ± 0.022	0.070 ± 0.025	0.003 ± 0.001
NGC 5024, M 53	0.790	0.100 ± 0.017	0.690 ± 0.017	0.263 ± 0.023	0.737	0.120 ± 0.019	0.617 ± 0.019	0.020 ± 0.013	0.006 ± 0.001
NGC 5053	0.790	0.116 ± 0.014	0.674 ± 0.014	0.320 ± 0.019	–	–	–	–	0.004 ± 0.001
NGC 5272, M 3$^{(a)}$	0.847	0.188 ± 0.017	0.659 ± 0.017	0.459 ± 0.023	0.789	0.240 ± 0.022	0.550 ± 0.022	0.052 ± 0.014	0.005 ± 0.001
NGC 5466	0.798	0.103 ± 0.017	0.695 ± 0.017	0.264 ± 0.023	0.788	0.119 ± 0.023	0.669 ± 0.023	0.016 ± 0.022	0.002 ± 0.001
NGC 5904, M 5	0.833	0.176 ± 0.021	0.657 ± 0.021	0.404 ± 0.029	0.782	0.216 ± 0.022	0.566 ± 0.022	0.040 ± 0.015	0.006 ± 0.001
NGC 5986	0.798	0.170 ± 0.019	0.628 ± 0.019	0.419 ± 0.026	0.756	0.263 ± 0.024	0.493 ± 0.024	0.093 ± 0.025	0.003 ± 0.001
NGC 6093, M 80	0.791	0.156 ± 0.021	0.635 ± 0.021	0.397 ± 0.029	0.755	0.266 ± 0.027	0.489 ± 0.027	0.110 ± 0.020	0.003 ± 0.001
NGC 6101	0.798	0.110 ± 0.015	0.688 ± 0.015	0.282 ± 0.020	0.775	0.120 ± 0.019	0.655 ± 0.019	0.010 ± 0.015	0.006 ± 0.001
NGC 6121, M 4$^{(b)}$	0.850	0.209 ± 0.024	0.624 ± 0.024	0.481 ± 0.023	0.833	0.236 ± 0.027	0.597 ± 0.027	0.027 ± 0.007	0.006 ± 0.001
NGC 6144	0.797	0.166 ± 0.019	0.631 ± 0.019	0.429 ± 0.026	0.775	0.176 ± 0.026	0.599 ± 0.026	0.010 ± 0.027	0.002 ± 0.001
NGC 6171, M 107	0.859	0.230 ± 0.025	0.629 ± 0.025	0.528 ± 0.034	0.823	0.243 ± 0.028	0.580 ± 0.028	0.013 ± 0.017	0.006 ± 0.001
NGC 6205, M 13	0.821	0.210 ± 0.020	0.611 ± 0.020	0.526 ± 0.027	0.750	0.273 ± 0.021	0.477 ± 0.021	0.063 ± 0.015	0.003 ± 0.001
NGC 6218, M 12	0.815	0.223 ± 0.023	0.592 ± 0.023	0.540 ± 0.032	0.799	0.270 ± 0.029	0.559 ± 0.029	0.047 ± 0.022	0.003 ± 0.001
NGC 6254, M 10	0.815	0.206 ± 0.019	0.609 ± 0.019	0.519 ± 0.026	0.775	0.233 ± 0.026	0.542 ± 0.027	0.026 ± 0.021	0.004 ± 0.001
NGC 6341, M 92	0.781	0.053 ± 0.020	0.728 ± 0.020	0.149 ± 0.027	0.730	0.120 ± 0.022	0.610 ± 0.022	0.067 ± 0.018	0.004 ± 0.001
NGC 6362	0.851	0.213 ± 0.025	0.638 ± 0.025	0.482 ± 0.034	0.845	0.250 ± 0.028	0.595 ± 0.028	0.037 ± 0.015	0.003 ± 0.001
NGC 6397	0.792	0.136 ± 0.015	0.659 ± 0.015	0.365 ± 0.020	0.781	0.146 ± 0.020	0.635 ± 0.020	0.010 ± 0.016	0.005 ± 0.001
NGC 6441	0.918	0.223 ± 0.016	0.695 ± 0.016	0.499 ± 0.025	0.795	0.296 ± 0.047	0.499 ± 0.047	0.073 ± 0.044	0.006 ± 0.001
NGC 6535	0.794	0.180 ± 0.021	0.614 ± 0.021	0.476 ± 0.029	0.790	0.203 ± 0.025	0.587 ± 0.025	0.023 ± 0.015	0.002 ± 0.001
NGC 6541	0.796	0.170 ± 0.016	0.626 ± 0.016	0.448 ± 0.022	0.736	0.220 ± 0.026	0.516 ± 0.026	0.050 ± 0.022	0.006 ± 0.001
NGC 6584	0.821	0.150 ± 0.019	0.671 ± 0.019	0.351 ± 0.026	0.800	0.166 ± 0.024	0.633 ± 0.024	0.016 ± 0.020	0.005 ± 0.001
NGC 6681, M 70	0.800	0.183 ± 0.018	0.617 ± 0.018	0.461 ± 0.025	0.761	0.256 ± 0.029	0.505 ± 0.029	0.073 ± 0.029	0.004 ± 0.001
NGC 6717, Pal 9	0.822	0.220 ± 0.022	0.602 ± 0.022	0.520 ± 0.030	0.818	0.256 ± 0.024	0.562 ± 0.024	0.036 ± 0.015	0.005 ± 0.001
NGC 6723	0.827	0.180 ± 0.023	0.647 ± 0.023	0.401 ± 0.032	0.793	0.233 ± 0.024	0.560 ± 0.024	0.053 ± 0.013	0.004 ± 0.001
NGC 6752	0.814	0.216 ± 0.022	0.598 ± 0.022	0.544 ± 0.030	0.756	0.276 ± 0.023	0.480 ± 0.023	0.060 ± 0.017	0.006 ± 0.001
NGC 6779, M 56	0.789	0.140 ± 0.015	0.649 ± 0.015	0.374 ± 0.020	0.747	0.173 ± 0.020	0.574 ± 0.020	0.033 ± 0.016	0.005 ± 0.001
NGC 6809, M 55	0.790	0.140 ± 0.017	0.650 ± 0.017	0.370 ± 0.023	0.756	0.173 ± 0.025	0.583 ± 0.025	0.033 ± 0.017	0.005 ± 0.001
NGC 6981, M 72	0.825	0.160 ± 0.022	0.665 ± 0.022	0.371 ± 0.030	0.801	0.183 ± 0.024	0.618 ± 0.024	0.023 ± 0.015	0.004 ± 0.001
NGC 7078, M 15	0.791	0.073 ± 0.021	0.718 ± 0.021	0.205 ± 0.029	0.700	0.210 ± 0.024	0.490 ± 0.024	0.137 ± 0.019	0.008 ± 0.001
NGC 7099, M 30	0.781	0.066 ± 0.014	0.715 ± 0.014	0.193 ± 0.019	0.752	0.083 ± 0.019	0.669 ± 0.019	0.017 ± 0.019	0.006 ± 0.001

ID	M^{Tip}_{1G} (M$_\odot$)	μ_{1G} (M$_\odot$)	$\bar{M}^{\text{HB}}_{1G}$ (M$_\odot$)	$\eta_{R,1G}$	M^{Tip}_{2G} (M$_\odot$)	μ_{2G} (M$_\odot$)	$\bar{M}^{\text{HB}}_{2G}$ (M$_\odot$)	$\Delta\mu_e$ (M$_\odot$)	δ (M$_\odot$)
NGC 0104, 47 Tuc	0.871	0.233 ± 0.045	0.638 ± 0.045	0.516 ± 0.059	0.859	0.233 ± 0.044	0.626 ± 0.044	–	0.004 ± 0.001
NGC 5927	0.919	0.263 ± 0.031	0.656 ± 0.031	0.601 ± 0.042	0.902	0.263 ± 0.033	0.632 ± 0.033	–	0.006 ± 0.001
NGC 6304	0.914	0.270 ± 0.031	0.644 ± 0.031	0.618 ± 0.042	0.900	0.270 ± 0.032	0.630 ± 0.032	–	0.004 ± 0.001
NGC 6352	0.909	0.256 ± 0.039	0.653 ± 0.039	0.583 ± 0.053	0.880	0.256 ± 0.041	0.624 ± 0.041	–	0.004 ± 0.001
NGC 6366	0.895	0.273 ± 0.041	0.622 ± 0.041	0.626 ± 0.056	–	–	–	–	0.003 ± 0.002
NGC 6496	0.924	0.280 ± 0.020	0.644 ± 0.020	0.644 ± 0.026	0.910	0.280 ± 0.023	0.634 ± 0.023	–	0.004 ± 0.001
NGC 6624	0.914	0.276 ± 0.014	0.638 ± 0.014	0.633 ± 0.018	0.898	0.276 ± 0.015	0.608 ± 0.015	–	0.005 ± 0.001
NGC 6637	0.881	0.253 ± 0.039	0.648 ± 0.039	0.575 ± 0.056	0.875	0.253 ± 0.042	0.621 ± 0.042	–	0.003 ± 0.001
NGC 6652	0.842	0.180 ± 0.031	0.662 ± 0.031	0.390 ± 0.042	0.832	0.180 ± 0.032	0.654 ± 0.032	–	0.004 ± 0.001
NGC 6838, M 71	0.858	0.210 ± 0.018	0.648 ± 0.018	0.466 ± 0.024	0.850	0.210 ± 0.020	0.640 ± 0.020	–	0.005 ± 0.001

In the next section, we further investigate the mass of HB 1G stars and the mass-loss of 1G stars, while Section 4.2 is dedicated to HB mass and mass-loss of 2Ge stars.

4.1 Mass-loss of first-generation stars

The results listed in Table 2, where we provide mass-losses for 1G stars of 46 GCs, show that the mass-loss of 1G stars clearly depends on the cluster metallicity. This fact is illustrated in Fig. 5(a), which shows a strong correlation between 1G mass-loss and the iron abundance.

The values of μ_{1G} and [Fe/H] of Fig. 5(a) follow the linear relation:

$$\mu_{1G} = (0.095 \pm 0.007) \times [\text{Fe/H}] + (0.313 \pm 0.012) \qquad (1)$$

obtained by means of least squares and represented with a black line in Fig. 5(a). The Pearson rank coefficient of this linear fit has the high value $R_p = 0.88$, showing that the points are well reproduced by a straight line. Nevertheless, the 1G mass-loss spread among GCs with the same iron abundance is larger than that expected based on the observational errors.
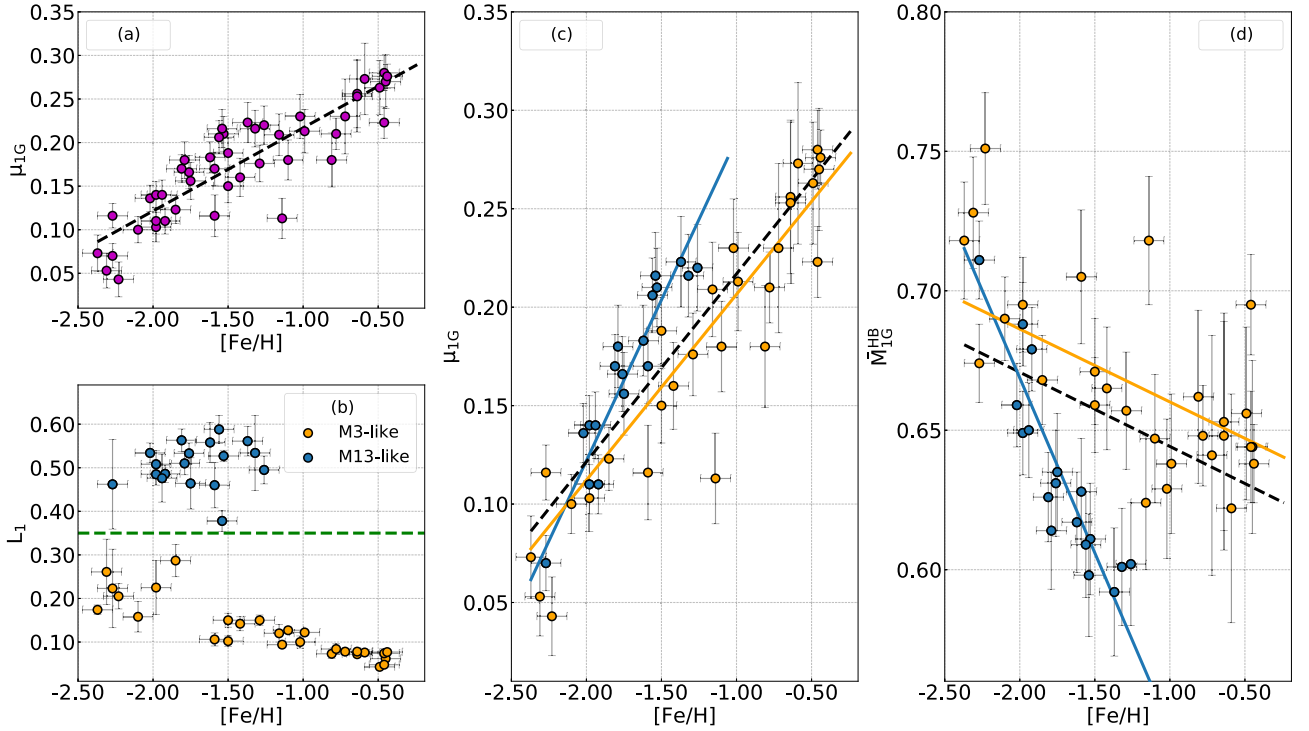
Figure 5. *Panel a:* Mass-loss of 1G stars, μ_{1G}, as a function of [Fe/H]. *Panel b:* Colour distance between the reddest part of the HB, L_1 (Milone et al. 2014), against [Fe/H]. The dashed line at $L_1 = 0.35$ mag separates the groups of M3- (orange) and M13-like (blue) GCs selected in this paper. *Panel c:* Same as panel *a* but with the two groups of GCs identified in panel *b* marked with the corresponding colours. *Panel d:* Average HB mass of 1G stars, $\bar{M}_{1G}^{HB}$, as a function of [Fe/H] for M3- (orange) and M13-like GCs (blue). The black dashed lines mark are the best-fitting straight lines derived from all the studied clusters, while blue and orange lines represent the best-fitting straight lines derived for M3- and M13-like clusters, respectively. The equations of these lines are provided in Table 3.

To investigate the reasons of this scatter, we analyse the two distinct groups of GCs selected in Fig. 5(b), where we plot the colour distance between the RGB and the reddest part of HB (L_1, Milone et al. 2014) against [Fe/H]. By adopting the names of the GC prototypes, M3 and M13, we define M3-like GCs with $L_1 \leq 0.35$, which mostly include GCs having HB stars on the red side of the RR Lyr region, and M13-like GCs with $L_1 > 0.35$, in which stars redder than the RR Lyr are missing.[2] The evidence that M13-like GCs provide different L_1 values than the remaining GCs with the same [Fe/H] reflects the fact that GCs with the same metallicity exhibit different HB morphologies, and that at least one second parameter, in addition to metallicity, is needed to explain the HB of GCs.

In Fig. 5(c) we show again the μ_{1G} versus [Fe/H] plot of panel a, highlighting the M3- (yellow dots) and M13-like (blue dots) clusters. Clearly, M13-like GCs lie on a steeper relation than M3-like GCs. The plot clearly shows the evidence coming out from the different HB morphology of the two groups: the 1G stars of M13-like GCs loose more mass than the 1G stars of M3-like GCs with the same metallicity, if no other parameter is at play.

4.1.1 HB and RGB-tip masses of 1G stars

To give a different look at the correlation between mass-loss of 1G stars and GC metallicity shown in Fig. 5(c), we analyse the dependence between [Fe/H], $\bar{M}_{1G}^{HB}$ and M_{1G}^{Tip}. Obviously, the mass-loss has been simply obtained as the difference between the mass at the RGB tip and the average HB mass.

Fig. 5(d) shows that the average HB masses of 1G stars vary in the range from ∼0.60 to ∼0.75 $M_\odot$.[3]

We also note a mild anticorrelation between $\bar{M}_{1G}^{HB}$ and [Fe/H], although clusters with similar metallicities span a wide range of HB masses, with M3- and M13-like GCs following distinct patterns in the $\bar{M}_{1G}^{HB}$ versus [Fe/H] plane. Specifically, 1G stars of M13-like clusters have smaller HB masses when compared with their counterparts of M3-like GCs. This latter group exhibits a broad distribution around the best-fitting least-squares line (yellow line in Fig. 5d) corresponding to a residual HB-mass spread of 0.025 $M_\odot$. In contrast, M13-like clusters show a small mass scatter of 0.015 $M_\odot$ around the corresponding best-fitting straight line (blue line).

On the contrary, the stellar masses of 1G stars at the RGB tip exhibit a strong correlation with [Fe/H] as illustrated in the top panel of Fig. 6, with M_{1G}^{Tip} ranging from less than 0.8 $M_\odot$ at [Fe/H] ∼ −2.4 to more than 0.9 $M_\odot$ in the most metal-rich studied GCs. Observations are reproduced by the red line, which is the best-fitting exponential function ($M_{1G}^{Tip} = (0.250 \pm 0.011) \times$

---

[2]M3-like objects include both the G1 and G2 groups defined by Milone et al. (2014), while the M13-like objects correspond to their G3 sample.

[3]We compared our results with other in the literature. For M 13 (NGC 6205), we obtain average mass-loss value in agreement with Dalessandro et al. (2013). Our average mass-loss value for NGC 0104 (47 Tuc) is in agreement within 1σ with the ones in di Criscienzo et al. (2010) and Salaris, Cassisi & Pietrinferni (2016). The average HB masses of 1G stars in 47 Tuc and M 13 are consistent with those derived by Denissenkov et al. (2017), while results on NGC 6809 and NGC 6362 are consistent with those by VandenBerg & Denissenkov (2018). Our results are not directly comparable with those by Jang et al. (2019), who assumed lower helium content ($Y = 0.23$) for 1G stars. Anyway, we notice that the values of M_{1G}^{HB} and μ_{1G} that they obtained for the GCs M4, M5, M15, and M80 are consistent with the conclusion that average HB masses and the mass-losses correlate with the cluster metallicity.
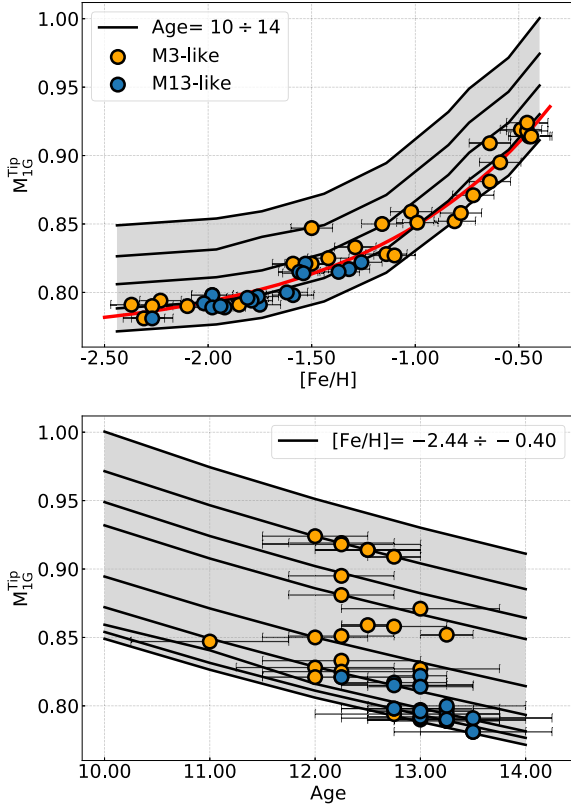
Figure 6. *Upper panel:* M_{1G}^{Tip} as function of iron abundance. The black solid lines correspond to ages of 10, 11, 12, 13, 14 Gyr with the oldest one located at the bottom. The red solid line is the least-square exponential fit of the data. *Lower panel:* Stellar mass of 1G stars at the tip of the RGB , M_{1G}^{Tip} provided by the best-fitting isochrones (from Tailo et al. 2016, 2017, 2019a, b), as function of GC age. Here, the black solid lines correspond to [Fe/H] −2.44, −1.96, −1.74, −1.44, −1.14, −0.84, −0.74, −0.55, −0.40 the lowest at the bottom.

$10^{(0.483\pm0.068)\times[Fe/H]} + (0.766 \pm 0.009))$ obtained by means of least squares.[4] Thus, the correlation between μ_{1G} and [Fe/H] comes out from the combination of the mild decrease of M_{1G}^{HB} (Fig. 5e) and the increase of M_{1G}^{Tip} with metallicity (Fig. 6).

To further explore HB 1G stars, we show in Fig. 7 the $\bar{M}_{1G}^{HB}$ versus [Fe/H] relations derived from the zero age HB models used in this paper for various effective temperatures. As expected, 1G stars of metal-rich clusters ([Fe/H]$\gtrsim$ −1.2) are, on average, cooler than those of metal-poor GCs. The 1G stars of M13-like GCs share similar effective temperatures (∼9000–12 000 K) and are typically hotter than the 1G stars if the M3-like GCs with similar [Fe/H]. This further reflects the effect of the still-debated second parameter on the HB of GCs.

4.2 Mass-loss in extreme second generation stars

RGB mass-loss and average HB masses of 2Ge stars significant vary from one cluster to another and both span an interval of about 0.25 M$_\odot$. Fig. 8 shows that these two quantities exhibit significant

---

[4]The scatter of the observed points around the red line is mostly due to the fact that, for a fixed metallicity, M_{1G}^{Tip} also depends on cluster age. Clearly, age dependence is small when compared to dependence from metallicity for the studied old GCs.
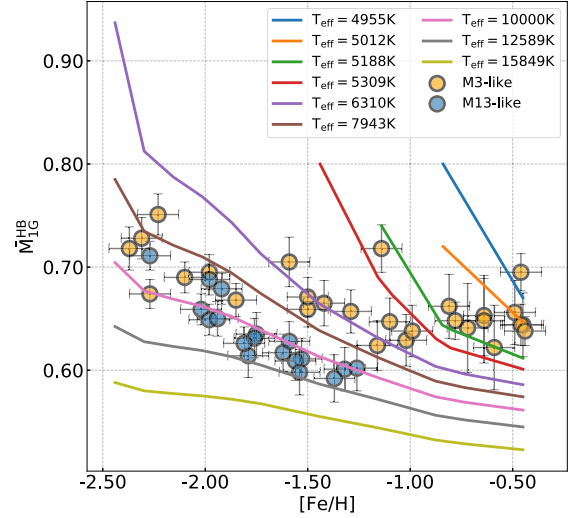
Figure 7. Reproduction of Fig. 5, where we show the average HB mass of 1G stars $\bar{M}_{1G}^{HB}$ as function of [Fe/H]. Here, we superimposed the curves from ZAHB models for different values of T_{eff}, as quoted in the inset.

correlation (μ_{2Ge}) and anticorrelation ($\bar{M}_{2Ge}^{HB}$) with [Fe/H], with metal-rich clusters having, on average smaller HB masses and higher mass-losses than metal-poor GCs. M3- and M13-like clusters are described by distinct linear correlations in both μ_{2Ge} versus [Fe/H] and $\bar{M}_{2Ge}^{HB}$ versus [Fe/H] planes, with M13-like GCs defining steeper slopes and larger scatters (Fig. 8). The comparison with Fig. 5 shows that mass-loss and HB masses of 1G and 2Ge stars share similar qualitative behaviours as function of [Fe/H].

As expected, 2Ge exhibit, on average, smaller HB masses and span a wider range of masses than the 2G and the 1Gs, as shown in Fig. 9, where we show the histogram distributions of $\bar{M}_X^{HB}$ (X = 1G, 2G, 2Ge).

2Ge stars also cover a wider mass-loss interval than the 1G, ranging from less than 0.05 to ∼ 0.30 M$_\odot$. This is illustrated in the left-hand panel of Fig. 10 where we compare the histogram distributions of μ_{1G} and μ_{2Ge} for GCs with the blue HB.

The histogram distribution of the mass-loss difference between 2Ge and 1G stars (right-hand panel of Fig. 10) shows that 2Ge stars of all GCs with blue HB lose more mass than 1G stars (i.e. $\Delta\mu_e > 0$). Hence, *additional mass-loss is required for the 2Ge to reproduce their location on the HB*. This result is emphasized in Fig. 11, where we plot the mass-loss of 2Ge stars as a function of the μ_{1G} (tan dots). Clearly, all GCs with blue HB lie above the dashed line, which is the locus of points with $\mu_{1G} = \mu_X$ (where X = 2G or 2Ge). On the contrary, we find that in clusters with only-red HB the same mass-loss properly reproduces the HB of both 1G and 2G stars.

We notice that several authors adopted enhanced mass-losses for their second-generation stars to reproduce the HB morphology, although this finding is not always explicitly highlighted in their papers. This fact includes work on both Galactic GCs (e.g. Dalessandro et al. 2011, 2013; Di Criscienzo et al. 2015; Denissenkov et al. 2017; Tailo et al. 2017; VandenBerg & Denissenkov 2018) and extragalactic GCs (e.g. D'Antona et al. 2013).

The mass-loss difference between 2Ge and 1G stars exhibits significant correlations with the maximum internal helium variation δY_{max} (Fig. 12), the present-day and initial masses[5] of the host GCs
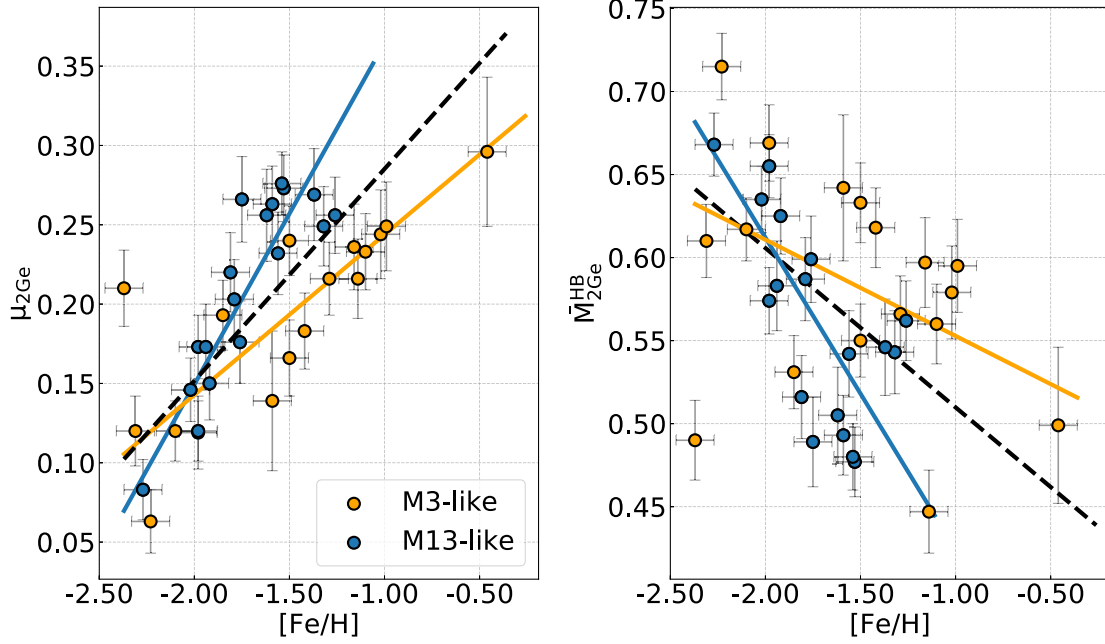
---

[5]From Baumgardt & Hilker (2018) and Baumgardt et al. (2019).

Figure 8. Mass-loss, (μ_{2Ge}, left-hand panel), and HB mass of 2Ge stars ($\bar{M}_{2Ge}^{HB}$, right-hand panel) against [Fe/H]. M3- and M13-like GCs identified in Fig. 5, are coloured orange and blue, respectively. The best-fitting straight lines derived from all GCs, and for M3- and M13 like clusters alone are coloured black, orange, and blue, respectively. Their equations are provided in Table 3.
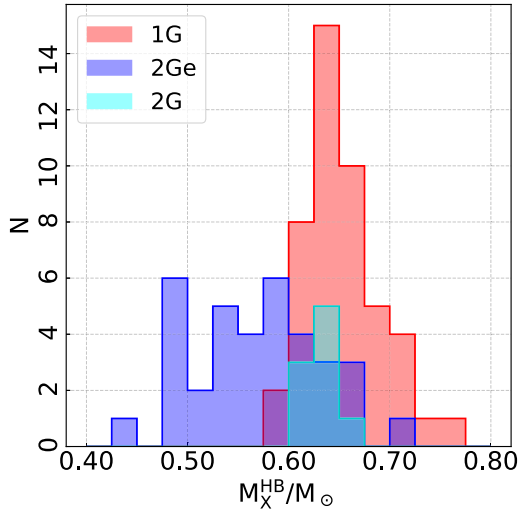

Figure 9. Histogram distributions of the average HB mass, M_X^{HB}, for all studied clusters. The histograms corresponding to X = 1G, X = 2Ge and, X = 2G are coloured, blue, red, and cyan, respectively.

(Fig. 13). M3- and M13-like GCs share similar patterns in all the panels of Fig. 12. On the other side, there is no evidence for significant correlation between $\Delta\mu_e$ and [Fe/H], as shown in Fig. 14.

5 DISCUSSION

The two main results of the analysis shown in Section 4 are as follows:

(i) There is a tight correlation between the average mass-loss of 1G stars and the GC metallicity; if we separate the 'second parameter' groups, the M13-like clusters follow a steeper relation than M3-like clusters.

(ii) The mass-loss of 2Ge stars is larger than the mass-loss of 1G stars, and this mass-loss difference is correlated with the helium abundance of the 2Ge stars and the mass of the host cluster.

In this section, we discuss these results in the context of their respective fields of stellar astrophysics. In Section 5.1, we compare the relation RGB 1G mass-loss versus [Fe/H] with the mass-loss resulting in models employing the Reimers' mass-loss expression (Reimers 1975, 1977). Section 5.2 is focused on the second-parameter problem of the HB morphology. Section 5.3 discusses the impact of the result of a larger mass-loss in the 2Ge on the formation scenarios of multiple stellar populations.

5.1 The mass-loss law

The problem of RGB mass-loss is certainly as old as the first attempts to interpret the features of GC CMDs. Fig. 5(a) shows a clear linear relation between μ_{1G} and [Fe/H]. This result depends on two main novelties of the present analysis: (1) we examined a large sample of GCs, *by means of an homogeneous set of data and models*; (2) in the multiple population framework, *we anchor the HB 1G stars to the coolest HB location in each cluster* which are then directly compared with the simulations. In this sense, our relation is a direct measurement of the mass-loss needed to describe the 1G stars.

Previous evidence that the mass-loss depends on the cluster has been provided in several papers. Gratton et al. (2010) show a strong relation between mass-loss and metallicity based on optical CMDs of a large sample of Galactic GCs. However, their results are based on the median mass of all HB stars and do not take the presence of MPs into account. As a consequence, the 'median' HB masses derived by Gratton and collaborators typically correspond to 2G stars, which are helium enhanced and hotter than the 1G and are higher than those derived in our paper from 1G stars. The difference is mostly due to the fact that the approach by Gratton et al. (2010) does not disentangle between the effect of helium abundance and
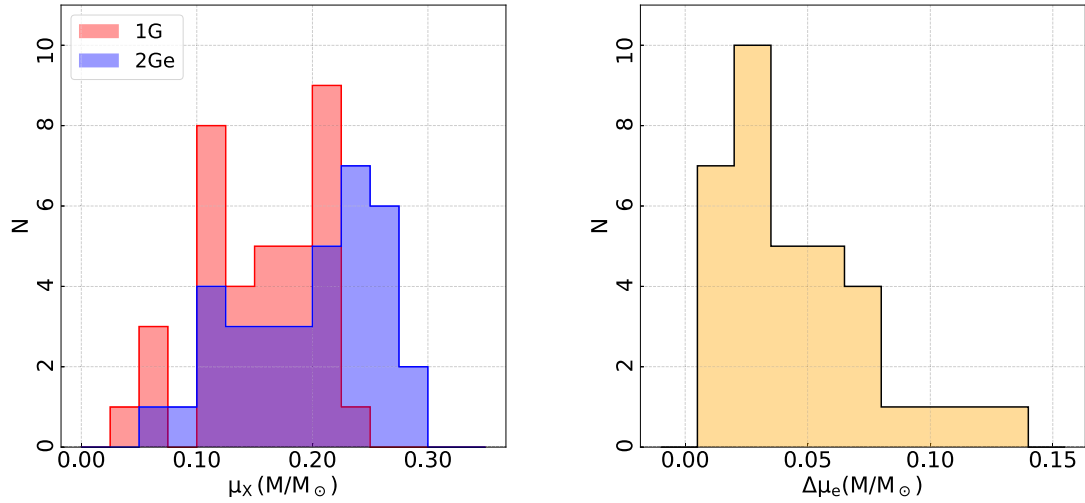
Figure 10. Histogram distributions of the mass-loss of 1G (red) and 2Ge stars (blue) in all clusters with blue HB (left) and histogram distribution of the differences between the mass-losses of 2Ge and 1G stars (right).
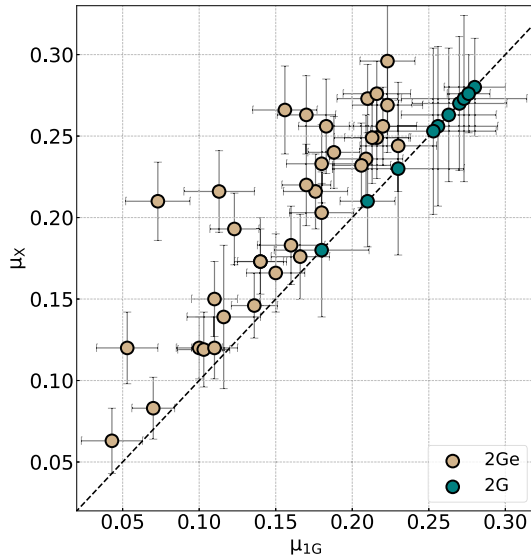

Figure 11. Average mass-loss of 2Ge stars (tan) or 2G stars (teal) as a function of the 1G average mass-loss. The black-dashed line represents the locus where $\mu_X = \mu_{1G}$.

Figure 12. Difference between the mass-loss of 2Ge and 1G stars, $\Delta\mu_e$, as a function of the maximum helium variation of the host GC. M3- and M13-like GCs are the orange and blue dots, respectively. The black, dashed line is the best least-squares fit: $\Delta\mu_e/M_\odot = (0.708 \pm 0.018) \times \delta Y_{max} + (0.018 \pm 0.003)$.

mass-loss on the median HB masses thus overestimating the amount of mass-loss. Origlia et al. (2014) inferred a similar relation between mass-loss and cluster metallicity by using Spitzer Infra Red Array Camera photometry obtained in the 3.6–8 μm of 16 GCs. Their results are based on mid-infrared excess of light in RGB stars, which was interpreted as the results of dust formation around these stars (but see Momany et al. 2012, for alternative interpretation in the case of 47 Tuc). Recently, Salaris et al. (2013) and Savino et al. (2019) have proposed a relation between mass-loss and metallicity from the study of the HB data of Sculptor and Tucana dwarf spheroidal galaxies, respectively. Both works involve direct comparisons of the observed HBs with synthetic HB stellar models.

For the sake of comparison, we report in Fig. 15 our equation (1) and the different relations listed above, with their 1σ intervals. Our relation is compatible with the one from Savino et al. (2019).

Historically, the mass-loss rate ($\dot{M}_*$, in M$_\odot$ yr^{-1}) of late-type giants has been described by Reimers (1975, 1977) formulation, given as $\dot{M}_* = 4 \times 10^{-13} \eta_R L_* R_* / M_*$ with L_*, R_*, M_* as stellar luminosity, radius, and mass, respectively, given in solar units, and η_R is a fitting parameter. In the left-hand panel of Fig. 16, we show the relations between mass-loss and [Fe/H] derived from the Reimers' law for η_R = 0.1, 0.3, and 0.6 (green, red, and purple colours). The continuous lines correspond to ages of 12 Gyr and the shaded areas enclose the mass-losses derived from models between 11 Gyr (upper boundaries) and 13 Gyr (lower boundaries). Clearly, the relations between 1G mass-loss and [Fe/H] derived from the observations are steeper than those expected from the Reimers' law for all the choices of η_R. We conclude that a constant value of η_R does not properly describe the mass-loss of 1G stars in GCs. We stress again that the relation we
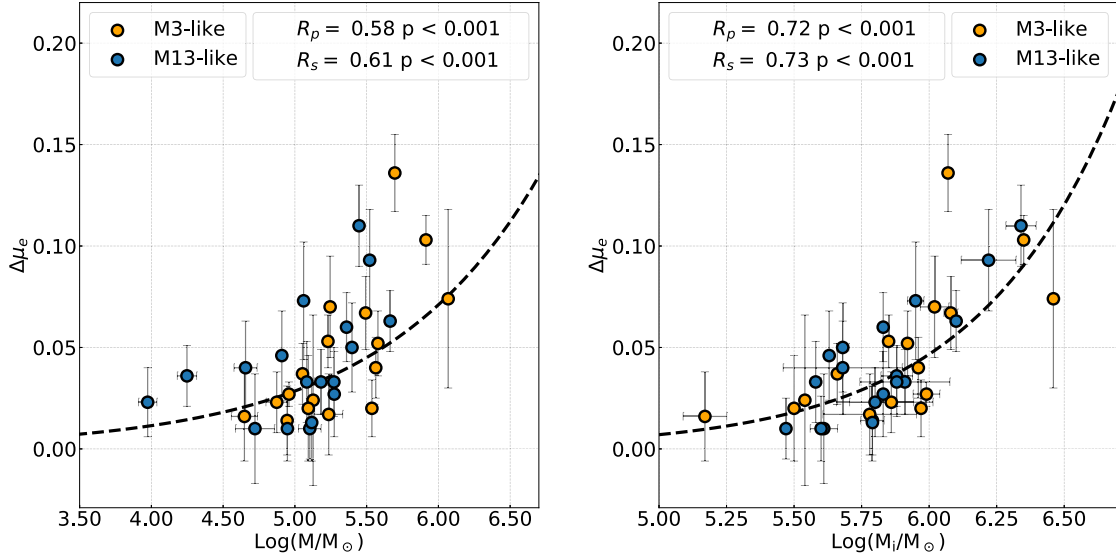
Figure 13. Difference between the mass-loss of 2Ge and 1G stars, $\Delta\mu_e$, as a function the present-day (left) and the initial GC mass (right). M3- and M13-like GCs are represented with orange and blue dots, respectively. Black dashed lines are derived by means of least-squares, and correspond to the relations that provide the best fit with the data: $\log(\Delta\mu_e/M_\odot) = (0.385 \pm 0.087) \times \log(M/M_\odot) - (3.469 \pm 0.445)$; $\log(\Delta\mu_e/M_\odot) = (0.823 \pm 0.143) \times \log(M_i/M_\odot) - (6.268 \pm 0.836)$..
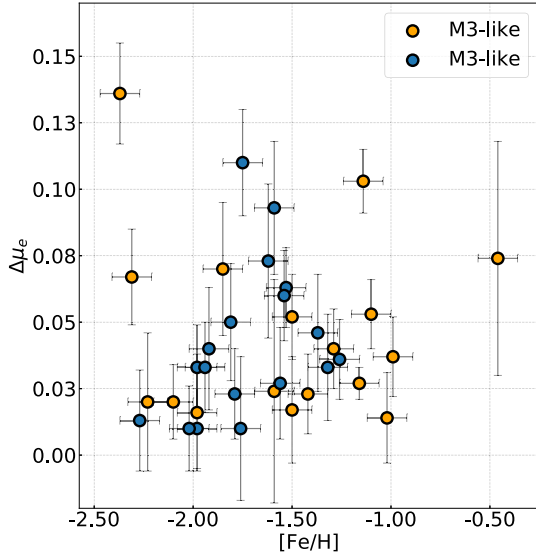
Figure 14. Difference between the mass-loss of 2Ge and 1G stars, $\Delta\mu_e$, against [Fe/H]. We colour the M3- and M13-like clusters identified in Fig. 5(b), orange and blue, respectively.

Figure 15. Comparison of μ_{1G} versus [Fe/H] relations found in this work with other relations in literature. The shaded areas are the 1σ interval of each relation, when available. Sources are Gratton et al. (2010, GR2010), Origlia et al. (2014, Or2014), Savino et al. (2019, Sv2019), and Salaris et al. (2013, Sl2013).

find refers to the 1G only, and not to the whole HB. Also recently, McDonald & Zijlstra (2015) find $\eta_R = 0.477 \pm 0.007$, a value independent of metallicity, because they select a 'median' HB mass, extracted from Gratton et al. (2010), to compute the RGB mass-loss.

A match with the observed μ_{1G} versus [Fe/H] relation can then be obtained by assuming a dependence between the fitting parameter η_R and the [Fe/H]. To do this, we estimate the value of η_R that reproduces mass-loss and metallicity of each GC, and plot in the right-hand panel of Fig. 16 η_R against [Fe/H]. η_R must increase with the cluster metallicity and we can describe mass-loss of 1G stars by the Reimers' formula with

$$\eta_R = (0.183 \pm 0.021) \times [\text{Fe/H}] + (0.682 \pm 0.032). \qquad (2)$$

The expression above is the least-squares best-fitting straight line derived from the points plotted in the right-hand panel of Fig. 16. Noticeably, M3- and M13-like GCs define different relations in the η_R versus [Fe/H] plane (see equations in Table 3).

5.2 Second parameter problem

In the following, we discuss the results of this paper in the context of the second-parameter of the HB morphology. Specifically, in Section 5.2.1 we discuss the impact of mass-loss of 1G stars in
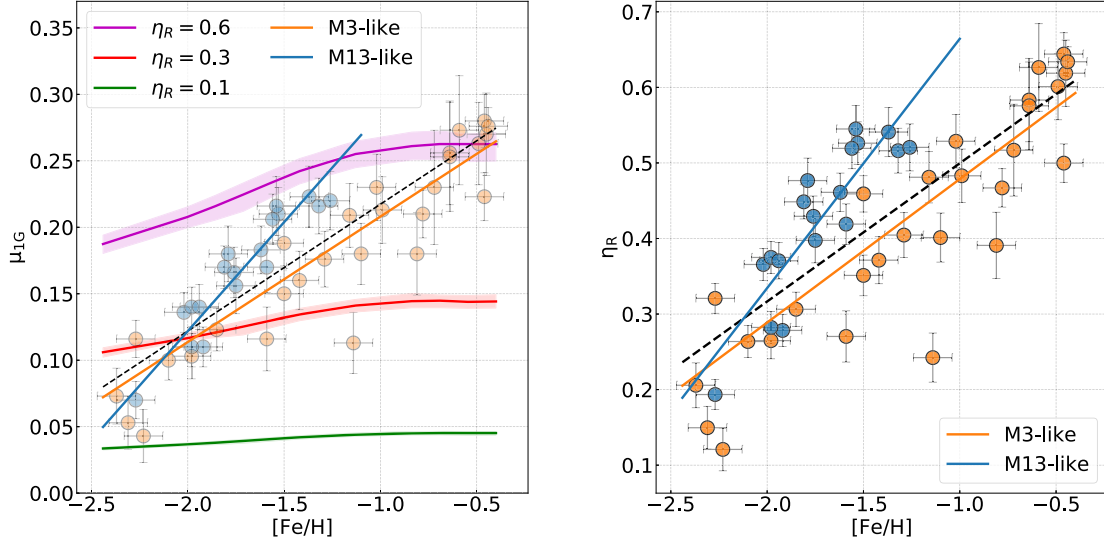
Figure 16. *Left-hand panel.* Reproduction of Fig. 5(a) where we show the 1G mass-loss against iron abundance for the studied GCs. The green, red, and purple lines are the mass-losses predicted by the Reimers'law for ages of 12 Gyr and $\eta_R = 0.1$, 0.3, and 0.6, respectively. The shaded areas include mass-losses for ages between 13 and 11 Gyr. See text for details. *Right-hand panel.* The value of η_R inferred for the 1G of each GC is plotted against cluster iron abundance. The black-dashed, blue, and orange lines of both panels represent the best-fitting straight lines derived for all GCs, and for M3- and M13-like GCs, respectively. Their equations are provided in Table 3.

Table 3. Linear fits in the form $\alpha \times$ [Fe/H] $+ \beta$ derived in this paper. We also provide the Pearson rank coefficient, R_P, and the r.m.s. of the residuals respect the best-fitting line.

Variable	ALL				M3-like				M13-like			
	α	β	R_P	Scatter	α	β	R_P	Scatter	α	β	R_P	Scatter
μ_{1G}	0.095 ± 0.007	0.313 ± 0.012	0.88	0.030	0.094 ± 0.007	0.302 ± 0.011	0.93	0.027	0.164 ± 0.015	0.450 ± 0.029	0.94	0.016
M_{1G}^{HB}	-0.027 ± 0.008	0.616 ± 0.014	-0.36	0.034	-0.027 ± 0.007	0.641 ± 0.010	-0.89	0.025	-0.126 ± 0.015	0.416 ± 0.029	-0.90	0.015
η_R	0.183 ± 0.021	0.682 ± 0.032	0.79	0.082	0.189 ± 0.018	0.672 ± 0.023	0.90	0.070	0.329 ± 0.044	0.994 ± 0.077	0.88	0.047
μ_{2Ge}	0.135 ± 0.018	0.421 ± 0.034	0.72	0.044	0.101 ± 0.021	0.345 ± 0.037	0.80	0.037	0.216 ± 0.023	0.581 ± 0.043	0.80	0.030
M_{2Ge}^{HB}	-0.097 ± 0.027	0.411 ± 0.049	-0.35	0.061	-0.059 ± 0.034	0.493 ± 0.062	-0.66	0.063	-0.190 ± 0.037	0.233 ± 0.068	-0.67	0.047

shaping the HB, while Section 5.2.2 is focused on the mass-loss difference between 2Ge and 1G stars.

5.2.1 1G mass-loss and HB morphology

The evidence that the mass-loss of 1G stars exhibits a strong correlation with the iron abundance of the host cluster confirms that metallicity is the first parameter in shaping the HB of GCs. The different HB morphology of the M3- and M13-like GCs, highlighted by the higher values of L1 (Milone et al. 2014) in the M13-like class, is the evidence that at least a second parameter is at play. Our analysis nicely shows (Fig. 5c) the straightforward result that M13-like GCs exhibit higher μ_{1G} than the other GCs with similar metallicity *if no other input is playing a role*. From the similar age determination for the clusters in our sample, we know that this second parameter cannot be the age.

If we apply to the M3- M13-like clusters the scenario that will be discussed in Section 5.3, the larger mass-loss of 1G stars in M13-like clusters may indicate that they formed in high-density environment compared to the 1G of M3-like GCs with the same metallicity.

It is worth to discuss two other possible scenarios:

(i) The 1G stars of the M13-like clusters may be born with a helium content larger than in the M3-like clusters. For example in the case of M 13, by combining the results in Section 4.1 with the

variation of M^{Tip} with helium, $\Delta M^{Tip} = -1.33 \times \delta Y$, obtained from our isochrones data base , we can reproduce the 1G HB stars by assuming an helium content $Y \sim 0.27$ and the same mass-loss of M3. Similar conclusion can be extended to all M13-like clusters. This scenario would imply that the 1G stars in this group of GCs originated from a primordial cloud that was already helium enhanced, but it would be challenging to explain the origin of such a high helium abundance in the gas at high redshift.

(ii) An intriguing explanation has been put forward by D'Antona & Caloi (2008) in their study of the second-parameter GC pair M 3-M 13. As predicted by various scenarios for the formation of multiple populations, GCs would lose a large amount of 1G stars as they evolve (see e.g. Renzini et al. 2015, and references therein). Hence, M13-like GCs could be extreme cases of clusters that have entirely lost their 1G. In this scenario, the stars that we used as 1G in M13-like GCs are actually fake-1G (see D'Antona & Caloi 2008; D'Antona et al. 2016, and references therein for details) and, as such, we can apply to them the scenario discussed below in Section 5.3, and suggest that have a small helium enhancement, to which we can associate and extra-mass-loss. Taking into account the '2G-like mass-loss', the helium needed to fit the cooler side of the HB in M 13 is a quite modest $Y \lesssim 0.26$, a value very close to the standard 1G value. These fake 1G stars, with a very modest helium enhancement, and correspondingly small or negligible abundance anomalies, are identified, for instance, in NGC 2808 as the stars of the 'population C'(D'Antona et al. 2016)
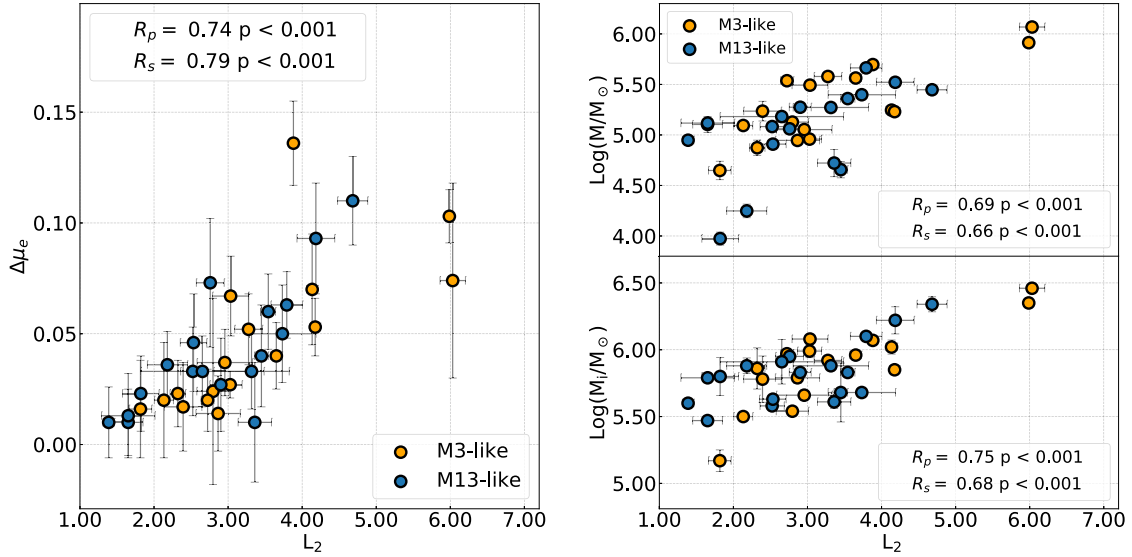
Figure 17. *Left-hand panel:* Difference between the mass-loss of 2Ge and 1G stars, $\Delta\mu_e$, against the $F275W - F814W$ colour extension of the HB. The groups of M3- and M13-like clusters are represented as orange and blue dots, as labelled. *Right-hand panel:* Present-day and initial cluster mass against the colour extension of the HB (top and bottom panels, respectively).

or with the population G1 in Kim & Lee (2018), and should be in fact the 2G populations closest in abundances to the 1G.

5.2.2 Enhanced mass-loss of 2Ge stars and HB morphology

When the presence of multiple populations in GCs was not yet clear, and researchers did not expect that the helium content of GC stars differ, even significantly, it was obvious that the more extended in colour was the HB, the larger had to be the mass-loss spread during the red giant evolution.

Introducing the helium content as a parameter of the morphology resulted to be a possible way to reduce this mass-loss spread, because, for fixed age and metallicity, helium-rich stellar populations exhibit bluer HBs than stellar populations with pristine helium content. It appeared possible to attribute to the enhanced helium the hotter locations along the HB (e.g. D'Antona et al. 2002, 2005; Gratton et al. 2010) and maybe get rid of the differences in mass-loss. This fact was also consistent with the strong correlation between the maximum helium variation derived from multiband photometry of GCs, and the colour extension of the HB (L2, Milone et al. 2014, 2018).

Nevertheless, here we found conclusively that helium variations alone are not able to entirely reproduce the observed HBs (see also Tailo et al. 2019a, b), and that extra-mass-loss is necessary to fit the observations. The left-hand panel of Fig. 17 shows that $\Delta\mu_e$ correlates with the colour extension of the HB (the parameter L2). The right-hand panel shows the correlation between L2 and the total present-day mass of clusters. Previous suggestions for the presence of such a type of correlation can be found in the literature, e.g. in Recio-Blanco et al. (2006) and Gratton et al. (2010). A similar correlation is found by adopting the initial masses (from Baumgardt et al. 2019). We conclude here that *the enhanced mass-loss of second-generation stars, together with helium variations are the parameters which determine the HB extension in GCs*, and both are related to the present-day and initial mass. In addition, we are driven to conclude that helium variations and extra-mass-loss may be two concomitant but different aspects of the formation of multiple populations, as we are going to outline in the next.

5.3 Extra-mass-loss in the 2Ge as a tracer of the multiple populations formation

The discovery that 2Ge stars of all GCs lose more mass than the 1G (Fig. 11, see also Tailo et al. 2015, 2019b, a) and, in particular, the correlations between the extra-mass-loss $\Delta\mu_e$ and the extra-helium content of the 2Ge population δY_{max} (Fig. 12) and the total (present-day and initial) mass of the clusters (Fig. 13) represent powerful constraints for the mechanisms of formation of multiple stellar populations. Since evolutionary effects alone cannot provide such increase (see Appendix D) the need of an additional mechanism arises, allowing us to gain information on the environment where the distinct generations were born.

Tailo et al. (2015) discuss, in the specific context of the blue hook morphology of ω Cen, how the formation environment of the different multiple populations can affect the stellar evolution during the RGB phase, mainly by affecting the initial stellar rotation. Here, we apply the same scenario to the less extreme environments encountered by the 2Ge of most clusters (see the schematic illustration in Fig. 18). Very young low-mass stars ($M/M_\odot \sim 0.1-1.0$) behave as the T-Tauri stars in the Galactic field, pre-main sequence stars in the convective phase of contraction towards the main sequence. T-Tauri's typically rotate with a period of 1–12 d, and their rotation rate is maintained constant in time by the magnetic coupling of the star with the accretion disc (magnetic disc-locking, see Armitage & Livio 1996). Bouvier et al. (1997a) and Bouvier, Forestini & Allain (1997b) developed a model to explain why main sequence stars in young clusters (such as α Persei) show a wide distribution of rotation velocities. They showed that, the earlier would pre-main sequence stars break the magnetic disc-locking, the faster would be their rotation when they reach the main sequence. Afterwards, during the main-sequence phase, the surface rotation rate (together with the rotation of the whole convective envelope) slows down thanks to the angular momentum loss associated with the stellar winds, but the core mostly preserves its fast rotation.

Rapid rotation affects the structure of the helium core, and delays the ignition of the helium core flash. This implies that, the faster the stellar core rotates, the more is the flash delayed, and the more time
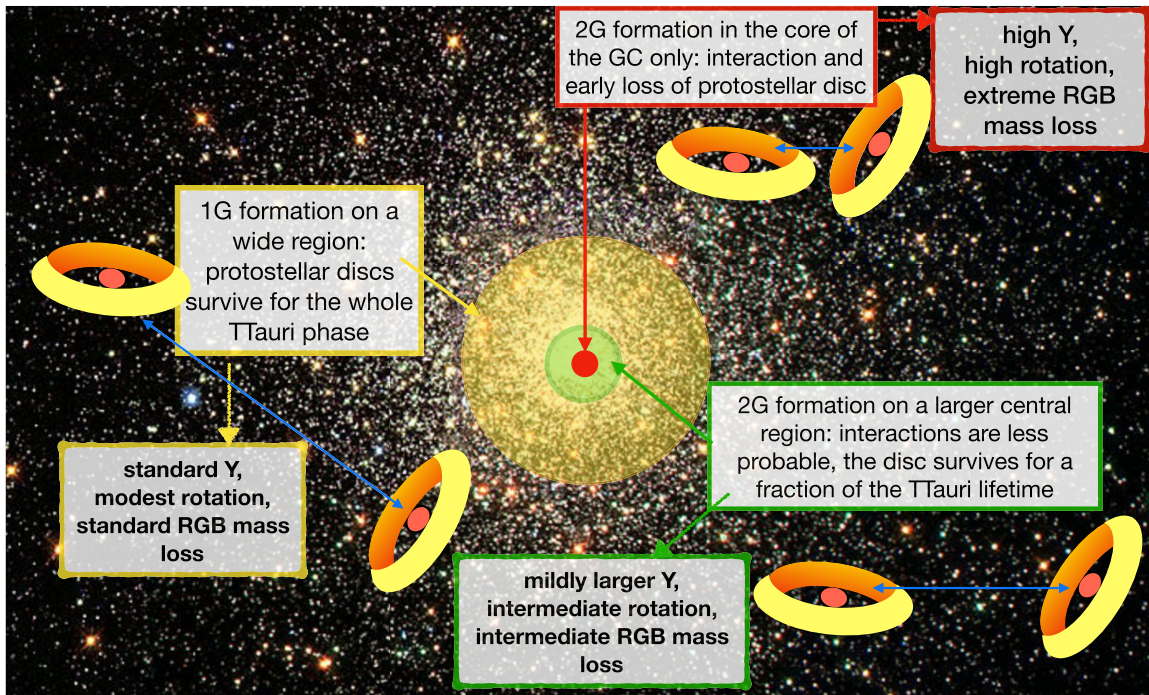
Figure 18. Schematic interpretation of the different rotation of 1G and 2G stars. During the pre-main-sequence evolution, the rotation of the central contracting star is magnetically locked to the rotation of its residual accretion disc, having a diameter of 50–100 au. While the 1G formation occurs in an ambient of moderate density (yellow region), where the disc–disc interactions occur on a time-scale longer than the typical stellar contraction time (few 10^6 yr), the 2G formation occurs in much smaller central regions (green and red regions, representing less and more extreme 2G populations; these regions represent either star formation in the same cluster at successive times, or star formation in clusters of different initial mass), where collisions and an early loss of the accretion disc are much more probable. Free stellar contraction and increase of the rotation rate follow the loss of the disc. Rapidly rotating cores delay ignition of the core-helium flash and allow a larger RGB mass-loss. This scheme, supported by hydrodynamical simulations, is at the basis of the direct correlation between the extra-mass-loss, the helium overabundance of the 2Ge populations, and the total initial mass of the cluster.

has the star to lose mass during the RGB evolution. Dispersion in core rotation within stars belonging to a GC was suggested, e.g. by Fusi-Pecci & Renzini (1978), to interpret the mass dispersion among the stars populating the HB (that is, the HB more or less extended morphology).

Here, we apply the key concept of this scenario in the context of the formation of multiple populations and propose that the different rotation rates and mass-loss may be the result the different formation environments for 1G and 2Ge. In fact, 2G stars form in denser environments in the innermost regions of a more extended 1G system (e.g. D'Ercole et al. 2008; D'Ercole, D'Antona & Vesperini 2016; Calura et al. 2019). A larger environment density implies more frequent star-to-star dynamical interactions able to destroy the stellar discs early enough, when the T Tauri radius is significantly larger than the final main sequence radius. The star is then free to contract while preserving its angular momentum at the time of detachment and, as the inertia momentum decreases, its rotation rate increases (see Tailo et al. 2015).

Hydro-dynamical simulations following the 2G formation show that the most extreme 2G stars (those less diluted with the environment gas, and thus preserving a larger helium content) are born in denser regions (e.g. Calura et al. 2019), where the stars may have shorter disc lifetime, gain higher rotation rates and eventually suffer larger mass-loss during the RGB evolution. On the other hand, less extreme 2G (those with a smaller helium enhancement formed with the dilution of processed gas and pristine gas), form less concentrated than the most extreme populations (see again Calura et al. 2019) and are thus subject to less frequent interactions during the pre-main sequence phase resulting in slower rotation and a smaller difference

in the RGB mass-loss. This scenario thus provides a possible explanation for the observed correlation between the $\delta Y_{\max}$ and $\Delta \mu_e$.

Fig. 13 shows that $\Delta \mu_e$ is also correlated with the clusters' present-day and initial masses. Although this correlation is not surprising in consideration of the fact that Milone et al. (2018) – their fig. 13 – found a very tight correlation between δY_{max} and the clusters' masses, it provides an additional hint concerning the key ingredients for the formation of multiple populations.

In the general context of the framework based on the pre-main sequence early-disc loss, the link between $\Delta \mu_e$, δY_{max} and cluster mass further strengthen the possibility of a fundamental connection between formation, very early dynamics and helium abundance of multiple populations. The simulations by Calura et al. (2019) show that, in general, more extreme 2G populations form more concentrated than the less extreme (more diluted) 2G population and this, in turn, as discussed above, is consistent with the correlation found in this study between δY_{max} and $\Delta \mu_e$. The additional link with the cluster's mass indicates that low-mass clusters tend to form less extreme populations (i.e. the 2Ge of low-mass clusters has smaller δY_{max} as indicated by the correlation between δY_{max} and the cluster's mass (Milone et al. 2018). This is a manifestation of an additional ingredient in the formation process: although this aspect certainly requires further investigation, we point out here that this trend is in general consistent with the model of pristine diluting gas re-accretion discussed in D'Ercole et al. (2016). In that framework, the dynamics of the early gas expulsion and re-accretion of pristine gas can lead to a more rapid re-accretion in low-mass clusters and the formation of a less extreme and less concentrated population compared to the more extreme and undiluted population forming in more massive clusters.

We conclude that the correlations of $\Delta\mu_e$ with the global parameters of the host clusters (helium content of the extreme population, present and initial mass of GC) are then fossil traces of the formation process, that can be explained in the framework of the formation of the 2G in more or less compact regions of the clusters. A schematic representation of this model is given in Fig. 18. Specific models of these cases, along the line of computation presented in Tailo et al. (2015), are planned for a future work.

We note, anyway, that Tailo et al. (2015) work was motivated by the necessity of explaining the peculiar shape of the blue hook stars in ω Cen. This required an extreme increase (up to $\sim 0.04\,M_\odot$) of the core mass at the helium flash, and therefore extreme values of main sequence rotation rate. In a more general scenario, we are considering a negligible increase of the core mass at flash, and a small increase of the luminosity at which the flash occurs, able to provide ~ 0.01–$0.05\,M_\odot$ more mass-loss (in most cases), corresponding to a small 2–5 per cent increase in RGB lifetime.

In the case of Fornax GCs, D'Antona et al. (2013) show that a main-sequence rotation rate of $\sim 70\,\mu$Hz is enough to increase mass lost by $\sim 0.03\,M_\odot$, in the approximation by Mengel & Gross (1976) and Renzini (1977). The models adopted for the estimate were based on the crude approximation of shell angular momentum conservation, which must be revised, based on the asteroseismic data for the core rotation of red giants presently available (Aerts, Mathis & Rogers 2019). Nevertheless, the low asteroseismic rotation velocities measured are at high variance also with the most recent models including the known mechanisms for the transport of angular momentum (e.g. Cantiello et al. 2014). There is only one star of low mass ($0.84\,M_\odot$) for which asteroseismic data have been analysed so far, the Kepler early red giant KIC 7341231 (Deheuvels et al. 2012). Interestingly, the authors find a core rotation of $\omega = 0.7\,\mu$Hz, a factor at least five times larger than the envelope rotation, but the rate is too low to be compatible with the available models. Nevertheless, it is quite possible that the evolution is different for the stars formed in dense stellar regions, such the 2G stars of GCs we are considering here, and there are no data available to rule out velocities a factor 100 larger needed by the model.

6 SUMMARY AND CONCLUSIONS

We combined high-precision photometry from the UV Legacy Survey of Galactic GCs (Piotto et al. 2015; Nardiello et al. 2018) and stellar population models to homogeneously analyse, for the first time, the HBs of a large sample of 46 clusters.

We identified candidate 1G, 2G, and 2Ge stars along the HB and inferred their mass-losses and average HB masses by following the recipe from pilot papers on M 3 and M 4 by Tailo et al. (2019a, b). In particular, we used helium abundances inferred by Milone et al. (2018) to fix the helium content of the 1G, 2G, and 2Ge stars and break the degeneracy between helium and mass-loss, which is one of the main challenges of HB studies.

The main results include the following:

(i) Mass-loss of 1G stars ranges from ~ 0.05 to $\sim 0.25\,M_\odot$ and correlates with the iron abundance of the host GCs. The resulting linear relation, which is described by equation (1), is not reproduced by the Reimers' mass-loss law for fixed η_R. We use our determinations of mass-loss to derive the *empirical law* that describes mass-loss in 1G stars of GCs, described by equation (2).

(ii) The strong correlation between μ_{1G} and [Fe/H] corroborates the evidence that metallicity is the main parameter of the HB morphology. The finding that the 1G of M13-like GCs have higher μ_{1G} values than 1G stars in M3-like GCs with similar metallicities, suggests that mass-loss, after metallicity is a second parameter that determines the HB shape. As an alternative, 1G stars of M13-like GCs are enhanced by ~ 0.01–0.03 in helium mass fraction and share the same mass-losses as the 1G of M3-like clusters. Otherwise following D'Antona & Caloi (2008), we speculate that M13-like clusters have entirely lost their true 1Gs. Hence, the stars that we call 1G are second-generation stars slightly enhanced in helium.

(iii) 2Ge stars of all studied GCs lose more mass than the corresponding 1Gs, thus confirming the conclusion by Tailo et al. (2015, 2017, 2019a, b) on ω Cen, NGC 6441, NGC 6388, M 4, and M 3. The mass-loss difference between 2Ge and 1G stars, $\Delta\mu_e$ correlates with the maximum internal helium variation and the mass of the host GC. Previous papers provided empirical evidence that the internal helium variation associated with multiple populations correlates with the colour extension of the HB. We show that helium variations alone do not entirely reproduce the observations, and that enhanced mass-loss of 2Ge stars, in addition to helium, is needed to explain the observed HBs. This finding provides further evidence that mass-loss, together with helium variation, is second parameter of the HB morphology.

(iv) Results on mass-loss may provide information on the formation environment of the distinct populations. The scenario proposed by Tailo et al. (2015) suggests that the accretion discs of pre-main-sequence 2Ge stars are disrupted at early stages by dynamical interactions in the dense environment of the innermost cluster regions. As a consequence, 2Ge stars exhibit faster rotation rates of the core and prolonged life as red giants, which result in the mass-loss increase. Our finding of high mass-loss in 2Ge stars relative to the 1G is consistent with this scenario and provide evidence that 2Ge stars formed in the dense cluster centres.

DATA AVAILABILITY

The photometric catalogues underlying this article are available in the *HST* UV legacy survey public data base (Piotto et al. 2015; Nardiello et al. 2018), at http://groups.dfa.unipd.it/ESPG/treasury.php. The models obtained via the ATON 2.0 code are not yet available to the public but they can be provided upon request.

REFERENCES

Aerts C., Mathis S., Rogers T. M., 2019, ARA&A, 57, 35
Armitage P. J., Livio M., 1996, ApJ, 470, 1024
Arp H. C., Baum W. A., Sandage A. R., 1952, AJ, 57, 4
Baumgardt H., Hilker M., 2018, MNRAS, 478, 1520

Baumgardt H., Hilker M., Sollima A., Bellini A., 2019, MNRAS, 482, 5138
Bouvier J. et al., 1997a, A&A, 318, 495
Bouvier J., Forestini M., Allain S., 1997b, A&A, 326, 1023
Brown T. M. et al., 2016, ApJ, 822, 44
Caloi V., D'Antona F., 2008, ApJ, 673, 847
Calura F., D'Ercole A., Vesperini E., Vanzella E., Sollima A., 2019, MNRAS, 489, 3269
Cantiello M., Mankovich C., Bildsten L., Christensen-Dalsgaard J., Paxton B., 2014, ApJ, 788, 93
D'Antona F., Caloi V., 2004, ApJ, 611, 871
D'Antona F., Caloi V., 2008, MNRAS, 390, 693
D'Antona F., Caloi V., Montalbán J., Ventura P., Gratton R., 2002, A&A, 395, 69
D'Antona F., Bellazzini M., Caloi V., Pecci F. F., Galleti S., Rood R. T., 2005, ApJ, 631, 868
D'Antona F., Caloi V., D'Ercole A., Tailo M., Vesperini E., Ventura P., Di Criscienzo M., 2013, MNRAS, 434, 1138
D'Antona F., Vesperini E., D'Ercole A., Ventura P., Milone A. P., Marino A. F., Tailo M., 2016, MNRAS, 458, 2122
D'Ercole A., Vesperini E., D'Antona F., McMillan S. L. W., Recchi S., 2008, MNRAS, 391, 825
D'Ercole A., D'Antona F., Carini R., Vesperini E., Ventura P., 2012, MNRAS, 423, 1521
D'Ercole A., D'Antona F., Vesperini E., 2016, MNRAS, 461, 4088
Dalessandro E., Salaris M., Ferraro F. R., Cassisi S., Lanzoni B., Rood R. T., Fusi Pecci F., Sabbi E., 2011, MNRAS, 410, 694
Dalessandro E., Salaris M., Ferraro F. R., Mucciarelli A., Cassisi S., 2013, MNRAS, 430, 459
Deheuvels S. et al., 2012, ApJ, 756, 19
Denissenkov P. A., VandenBerg D. A., Kopacki G., Ferguson J. W., 2017, ApJ, 849, 159
di Criscienzo M., Ventura P., D'Antona F., Milone A., Piotto G., 2010, MNRAS, 408, 999
Di Criscienzo M., Tailo M., Milone A. P., D'Antona F., Ventura P., Dotter A., Brocato E., 2015, MNRAS, 446, 1469
Dodge Y., 2008, The Concise Encyclopedia of Statistics. Springer, New York, p. 68
Dotter A. et al., 2010, ApJ, 708, 698
Dotter A., Sarajedini A., Anderson J., 2011, ApJ, 738, 74
Forbes D. A., Bridges T., 2010, MNRAS, 404, 1203
Fusi Pecci F., Ferraro F. R., Bellazzini M., Djorgovski S., Piotto G., Buonanno R., 1993, AJ, 105, 1145
Fusi-Pecci F., Renzini A., 1978, in Philip A. G. D., Hayes D. S., eds, Proc. IAU Symp. 80, The HR Diagram – The 100th Anniversary of Henry Norris Russell. Cambridge univeristy press, Cambridge, p. 225
Gratton R. G., Carretta E., Bragaglia A., Lucatello S., D'Orazi V., 2010, A&A, 517, A81
Grundahl F., Catelan M., Landsman W. B., Stetson P. B., Andersen M. I., 1999, ApJ, 524, 242
Harris W. E., 1996, AJ, 112, 1487
Iben I., Renzini A., 1984, Phys. Rep., 105, 329
Jang S., Kim J. J., Lee Y.-W., 2019, ApJ, 886, 116
Kim J. J., Lee Y.-W., 2018, ApJ, 869, 35
Kruijssen J. M. D., Pfeffer J. L., Reina-Campos M., Crain R. A., Bastian N., 2019, MNRAS, 486, 3180
Lagioia E. P. et al., 2018, MNRAS, 475, 4088
Lagioia E. P., Milone A. P., Marino A. F., Cordoni G., Tailo M., 2019, AJ, 158, 202
Mackey A. D., van den Bergh S., 2005, MNRAS, 360, 631
Marín-Franch A. et al., 2009, ApJ, 694, 1498
Marino A. F., Villanova S., Piotto G., Milone A. P., Momany Y., Bedin L. R., Medling A. M., 2008, A&A, 490, 625
Marino A. F., Villanova S., Milone A. P., Piotto G., Lind K., Geisler D., Stetson P. B., 2011, ApJ, 730, L16
Marino A. F. et al., 2014, MNRAS, 437, 1609
Marino A. F. et al., 2017, ApJ, 843, 66
McDonald I., van Loon J. T., 2007, A&A, 476, 1261

McDonald I., Zijlstra A. A., 2015, MNRAS, 448, 502
Mazzitelli I., D'Antona F., Ventura P., 1999, A&A, 348, 846
Mengel J. G., Gross P. G., 1976, Ap&SS, 41, 407
Milone A. P. et al., 2012a, A&A, 540, A16
Milone A. P. et al., 2012b, ApJ, 744, 58
Milone A. P. et al., 2014, ApJ, 785, 21
Milone A. P. et al., 2015, ApJ, 808, 51
Milone A. P. et al., 2017, MNRAS, 464, 3636
Milone A. P. et al., 2018, MNRAS, 481, 5098
Milone A. P. et al., 2020, MNRAS, 491, 515
Momany Y., Saviane I., Smette A., Bayo A., Girardi L., Marconi G., Milone A. P., Bressan A., 2012, A&A, 537, A2
Nardiello D. et al., 2018, MNRAS, 481, 3382
Origlia L., Ferraro F. R., Fabbri S., Fusi Pecci F., Dalessandro E., Rich R. M., Valenti E., 2014, A&A, 564, A136
Piotto G. et al., 2015, AJ, 149, 91
Recio-Blanco A., Aparicio A., Piotto G., de Angeli F., Djorgovski S. G., 2006, A&A, 452, 875
Reimers D., 1975, Mem. Soc. R. Sci. Liege, 8, 369
Reimers D., 1977, A&A, 57, 395
Renzini A., 1977, in Bouvier P., Maeder A., eds, Saas-Fee Advanced Course 7, Advanced Stages in Stellar Evolution, given at the Swiss Society for Astronomy and Astrophysics (SSAA). Observatoire de Genève, Switzerland, p. 151
Renzini A. et al., 2015, MNRAS, 454, 4197
Salaris M., de Boer T., Tolstoy E., Fiorentino G., Cassisi S., 2013, A&A, 559, A57
Salaris M., Cassisi S., Pietrinferni A., 2016, A&A, 590, A64
Sandage A., Wildey R., 1967a, ApJ, 150, 469
Sandage A., Wildey R., 1967b, ApJ, 150, 469
Savino A., Tolstoy E., Salaris M., Monelli M., de Boer T. J. L., 2019, A&A, 630, A116
Tailo M., 2016, Mem. Soc. Astron. Ital., 87, 654
Tailo M. et al., 2015, Nature, 523, 318
Tailo M., Di Criscienzo M., D'Antona F., Caloi V., Ventura P., 2016, MNRAS, 457, 4525
Tailo M. et al., 2017, MNRAS, 465, 1046
Tailo M., D'Antona F., Caloi V., Milone A. P., Marino A. F., Lagioia E., Cordoni G., 2019a, MNRAS, 486, 5895
Tailo M., Milone A. P., Marino A. F., D'Antona F., Lagioia E. P., Cordoni G., 2019b, ApJ, 873, 123
Torelli M. et al., 2019, A&A, 629, A53
VandenBerg D. A., Denissenkov P. A., 2018, ApJ, 862, 72
VandenBerg D. A., Brogaard K., Leaman R., Casagrand e L., 2013, ApJ, 775, 134
VandenBerg D. A., Denissenkov P. A., Catelan M., 2016, ApJ, 827, 2
Ventura P., D'Antona F., 2010, MNRAS, 402, L72
Ventura P., Zeppieri A., Mazzitelli I., D'Antona F., 1998, A&A, 334, 953
Zennaro M., Milone A. P., Marino A. F., Cordoni G., Lagioia E. P., Tailo M., 2019, MNRAS, 487, 3239

APPENDIX A: THE ANALYSED HB SAMPLE

We show in Figs A1–A4 the HBs of the 44 GCs analysed in this work. Each panel in the collection represents the CMD of the HB stars in each GC, in the $m_{F438W} - m_{F814W}$ versus m_{F814W} bands. We represent the best-fitting simulations for the 1G and the 2Ge as the red and blue contour plots, respectively. If the GC has only red HB stars (as in the case of NGC 6637), the blue contour plot refers to the 2G as a single group. The label in each panel reports the value of μ for the two stellar populations and, when relevant, the difference between these value ($\Delta\mu_e$). The different GCs are listed following their NGC number for an easier identification. For the cases of NGC 6121 and NGC 5272, which bring our total sample to 46 GCs, we refer to Tailo et al. (2019b, a), respectively.
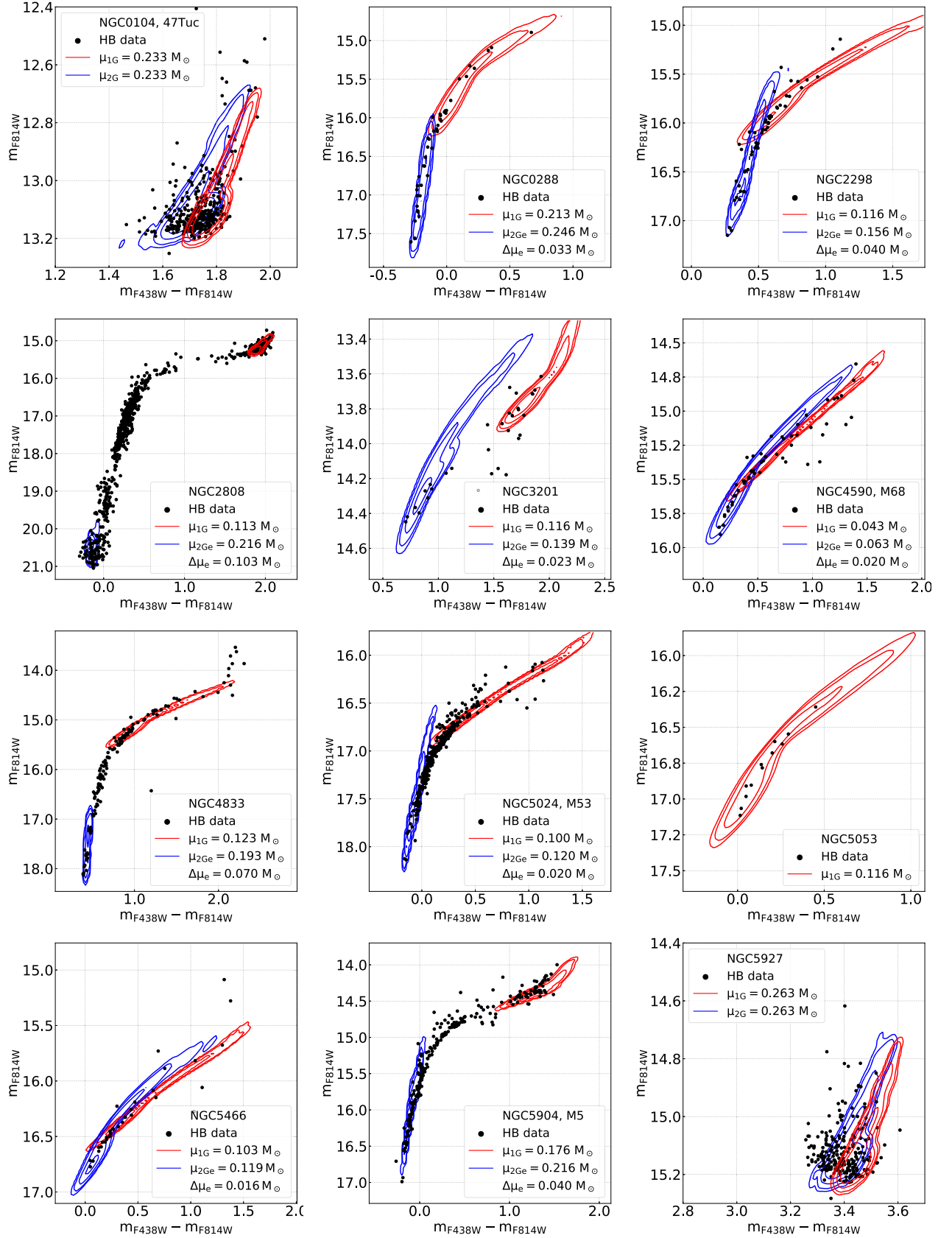
Figure A1. The analysed GCs sorted by catalogue number. We superimpose the best-fitting simulations of 1G and 2Ge or 2G HB stars on the observed CMDs of NGC 0104 (47 Tuc), NGC 0288, NGC 2298, NGC 2808, NGC 3201, NGC 4590 (M 68), NGC 4833, NGC 5024 (M 53), NGC 5053, NGC 5466, NGC 5909 (M 5), and NGC 5927. The average mass-losses of 1G and 2Ge (or 2G) stars are provided in the insets together with the corresponding mass-loss difference.
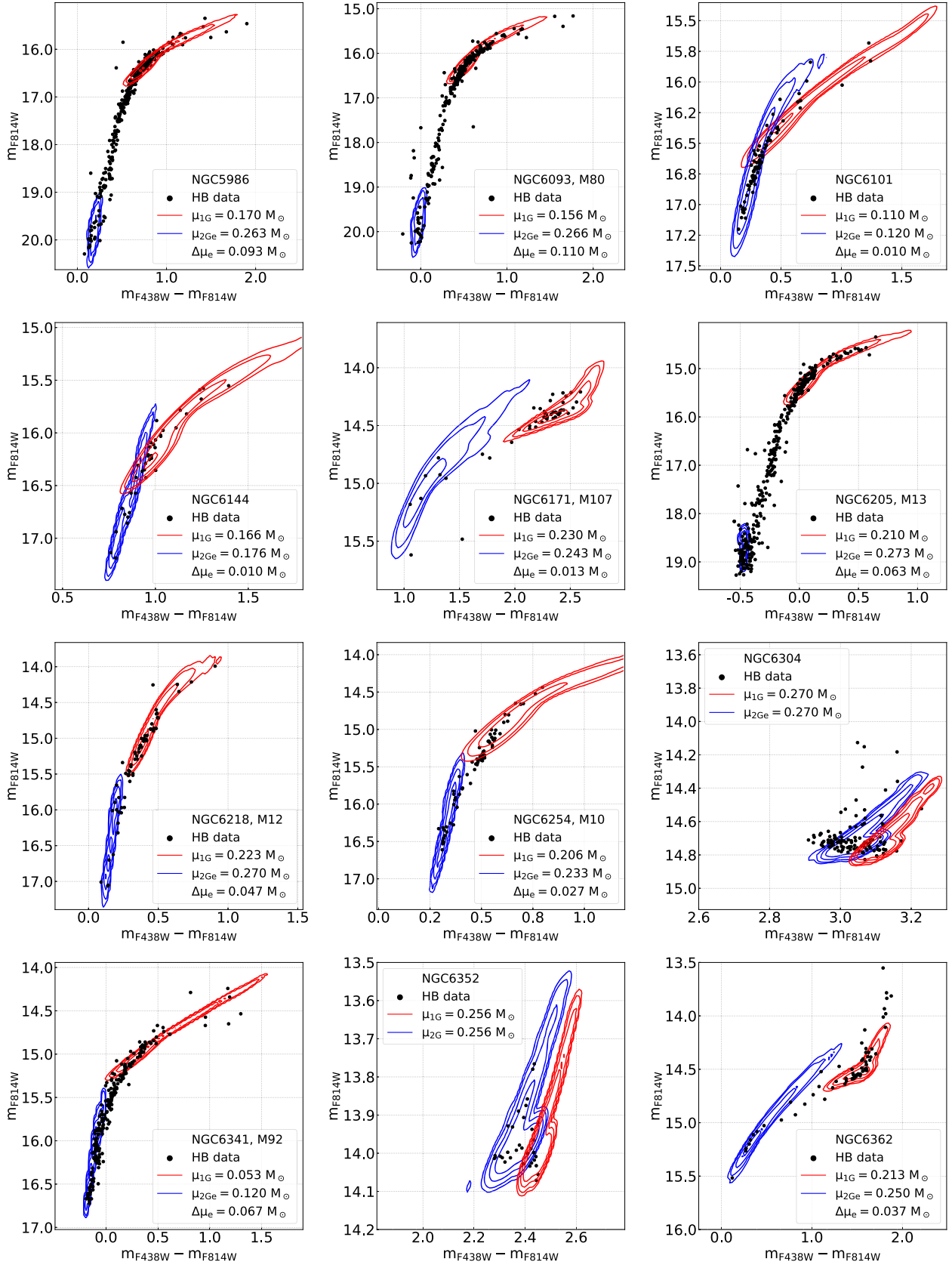
Figure A2. As Fig. A1 for NGC 5986, NGC 6093 (M 80), NGC 6101, NGC 6144, NGC 6171 (M 107), NGC 6205 (M 13), NGC 6218 (M 12), NGC 6254 (M 10), NGC 6304, NGC 6341 (M 92), NGC 6352, and NGC 6362.
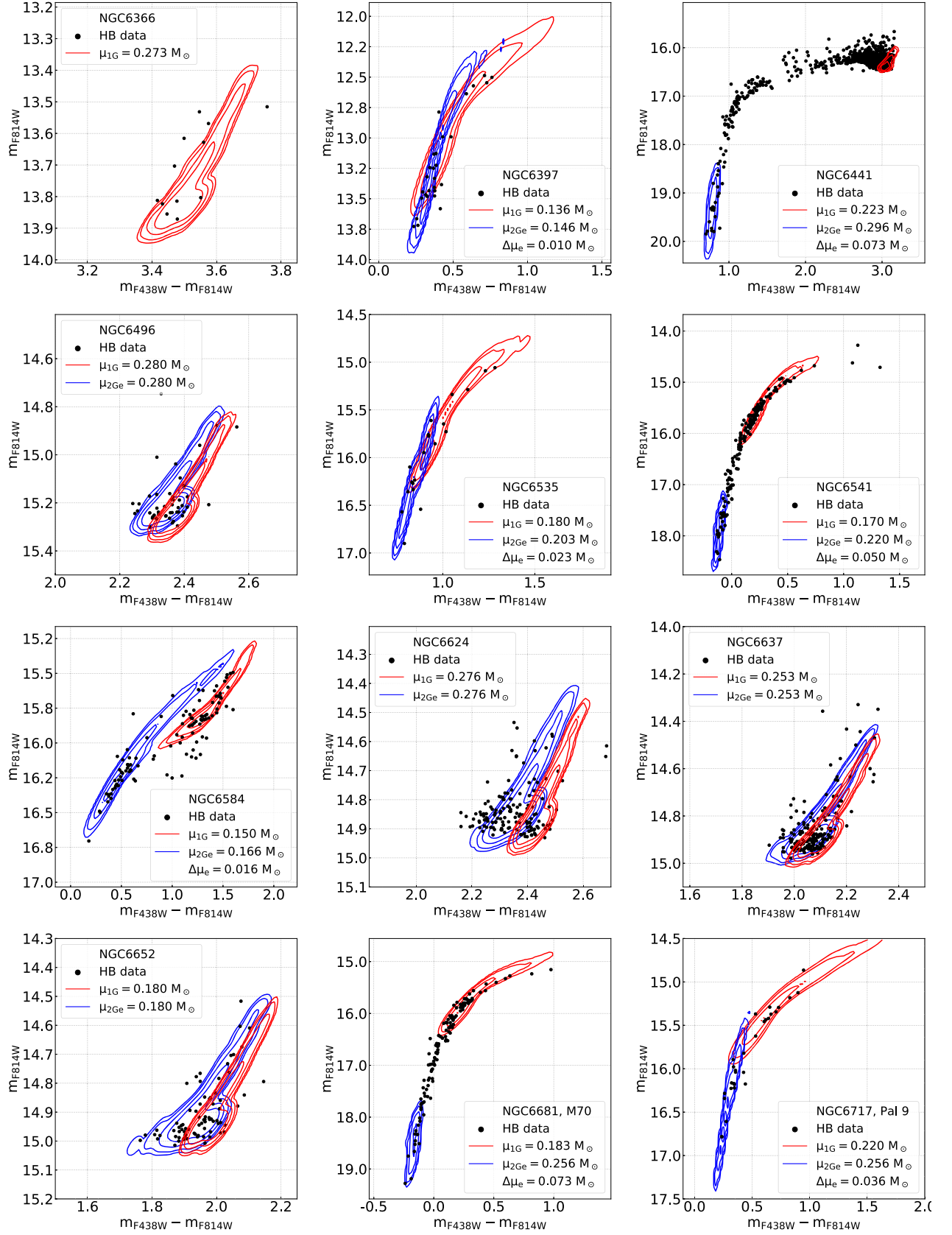
Figure A3. As Fig. A1 for NGC 6366, NGC 6397, NGC 6441, NGC 6496, NGC 6535, NGC 6541, NGC 6584, NGC 6624, NGC 6637, NGC 6652, NGC 6681 (M 70) and NGC 6717 (Pal 9).
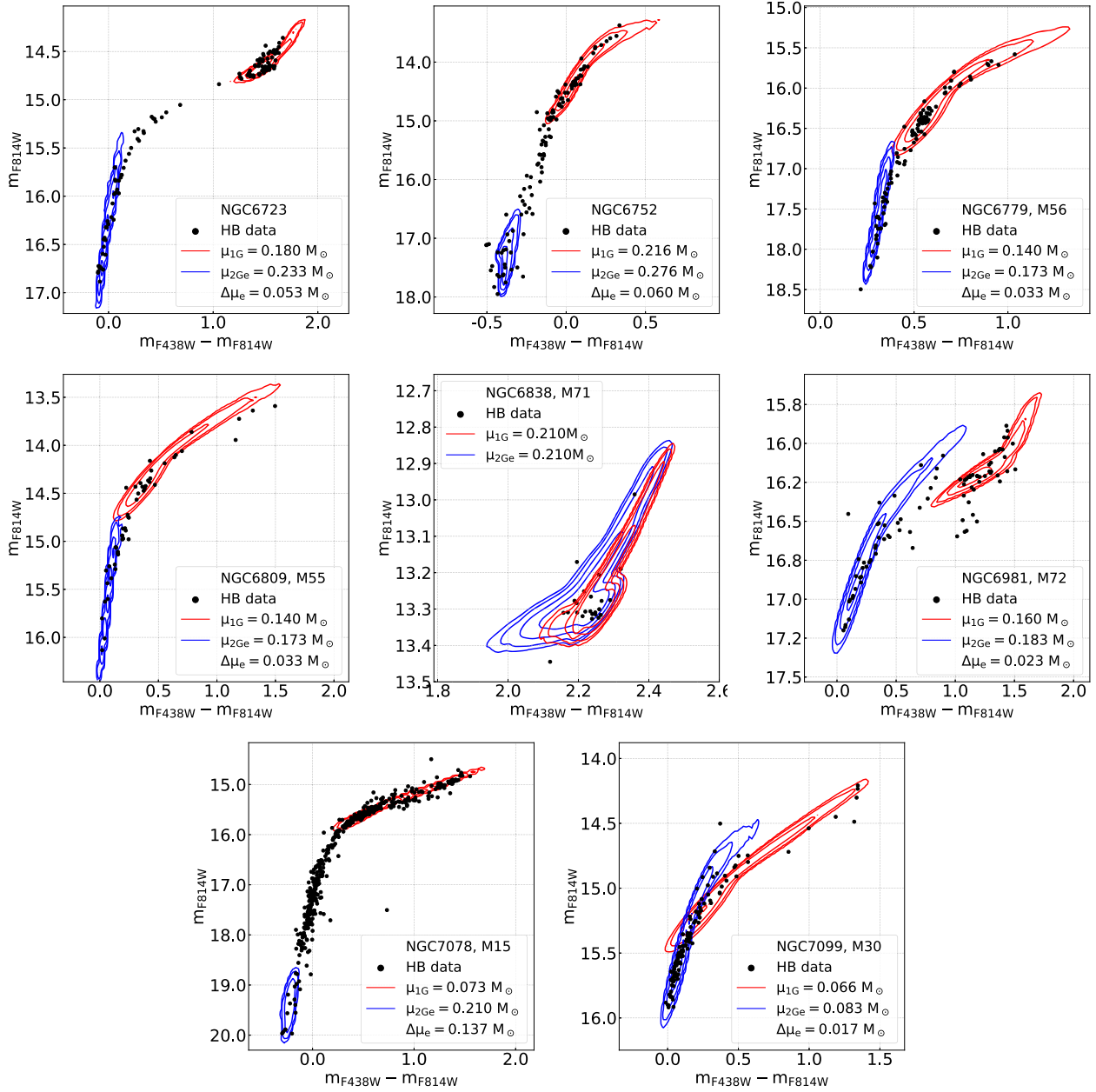
Figure A4. As Fig. A1 for NGC 6723, NGC 6752, NGC 6779 (M 56), NGC 6809 (M 55), NGC 6838 (M 71), NGC 6981 (M 72), NGC 7078 (M 15), and NGC 7099.

APPENDIX B: BI-VARIATE RELATIONS WITH GC PARAMETERS

In the main paper, we investigated the correlations between mass-loss, average HB mass of 1G and 2Ge stars, and some parameters of the host GCs. For completeness, we provide in the following the results of a bi-variate analysis that involves the 56 GC parameters that are listed in Table B1. Specifically, we provide the results on the correlations between μ_{1G}, μ_{2Ge}, $(\bar{M}_{1G}^{HB}, \bar{M}_{2Ge}^{HB}, \Delta\mu_e)$ and the cluster parameters in correlation maps provided in Fig. B1 (B2, B3, B4, B5).

For each couple of parameters, we provide the Spearman rank coefficient (R_S) and the p-value, which are indicative of the significance of the correlation, and the number of degrees of freedom. The colour of each cell (Figs B1–B5) is indicative of the value of R_S as indicated

by the colour bar. The correlations that, according to their p-value have low significance ($p > 0.05$).

The strongest correlation described in Fig. B1 involves μ_{1G} and the iron abundance as discussed in the main text. We also find significant correlations with the RGB width in the $F275W − F814W$ colour and the $C_{F275W,F336W,F438W}$ and $C_{F336W,F438W,F814W}$ pseudo-colours, which are quite expected because these quantities correlates with cluster metallicity (Milone et al. 2017; Lagioia et al. 2019). μ_{1G} anticorrelates with cluster ages as a consequence of the age–metallicity relation. Other correlations involve R_{GC}, R_{apog}, the slope of the MF slope and r_t ($R_S = −0.51$). As illustrated in Fig. B2, similar conclusion can be extended to the mass-loss of 2Ge stars.

The average mass-loss of 1G stars show some correlations with R_{apog}, R_{GC}, MF, slope and r_t (Fig. B3). The mass-loss

Table B1. Summary of the GC parameters we exploit in this work, together with the symbol we associate them, and their source. The source references are the following: (a) Milone et al. ([2018](#)); (b) Marín-Franch et al. ([2009](#)); (c) Dotter et al. ([2010](#)); (d) VandenBerg et al. ([2013](#)); (e) Mackey & van den Bergh ([2005](#)); (f) Harris ([1996](#), in its 2003 and 2010 version); (g) Milone et al. ([2014](#)); (h) Milone et al. ([2012a](#)); (i) Milone et al. ([2017](#)); (l) Lagioia et al. ([2019](#)); (m) Torelli et al. ([2019](#)); (n) Baumgardt & Hilker ([2018](#)); (o) Baumgardt et al. ([2019](#)).

Parameter name	Abbr.	Parameter name	Abbr.
Helium enhancement of the 2G (a)	$\delta Y_{2G,1G}$	Helium enhancement of the 2Ge (a)	$\delta Y_{2G,1G}$
Relative age (b)	Age	Age (c)	–
Age (d)	–	Horizontal branch ratio (e)	HBR
Iron over hydrogen ratio (f)	[Fe/H]	Reddening (f)	$E(B-V)$
Integrated visual absolute magnitude (f)	M_V	Concentration (f)	c
Luminosity density at the centre (f)	ρ_0	Central surface brightness (f)	SB_0
Projected ellipticity of isophotes (f)	ϵ	Specific RRLyrae density (f)	S_{RR}
Distance of the rHB from the RGB (g)	L_1	HB length (g)	L_2
Binary ($q > 0.5$) fraction in the core (h)	$f_{bin,c}$	Binary ($q > 0.5$) fraction between the core and the half mass radius (h)	$f_{bin,hm}$
Binary ($q > 0.5$) fraction outside the half mass radius (h)	$f_{bin,ohm}$	1G star ratio (i)	N_{1G}/N_T
RGB width in $m_{F275W} - m_{F814W}$ (i)	W_{F275W}	RGB width in $C_{F275W,F336W,F438W}$ (i)	$W_{C,F275W}$
RGB width in $C_{F275W,F336W,F438W}$ without [Fe/H] dependence (i)	$\Delta W_{C,F275W}$	RGB width in $C_{F336W,F438W,F814W}$ (l)	$W_{C,F336W}$
RGB width in $C_{F336W,F438W,F814W}$ without [Fe/H] dependence (l)	$\Delta W_{C,F336W}$	Ratio between CND in I and V–I bands (m)	τ_{HB}
Mass of the cluster (n)	M	Initial mass of the cluster (o)	M_i
Mass luminosity ratio in the V band (n)	M/L	Core radius (n)	r_c
Projected half light radius (n)	r_{hl}	Half mass radius (n)	r_{hm}
Tidal radius (n)	r_t	Mass function slope (n)	MF slope
Core density (n)	ρ_c	Density within the half mass radius (n)	ρ_{hm}
Relaxation time at half mass (n)	T_{rh}	Mass fraction of the dark remnants (n)	F_{remn}
Central velocity dispersion (n)	σ_0	Central escape velocity (n)	v_{esc}
Mass segregation coefficient in the core (n)	η_c	Mass segregation coefficient within the half mass radius (n)	η_c
Distance from the Galactic centre (o)	R_{GC}	Mean heliocentric velocity (o)	RV
Apogalacticon radius (o)	R_{apog}	Perigalacticon radius (o)	R_{perig}
Position components (o)	(X, Y, Z)	Velocity components (o)	(U, V, W)
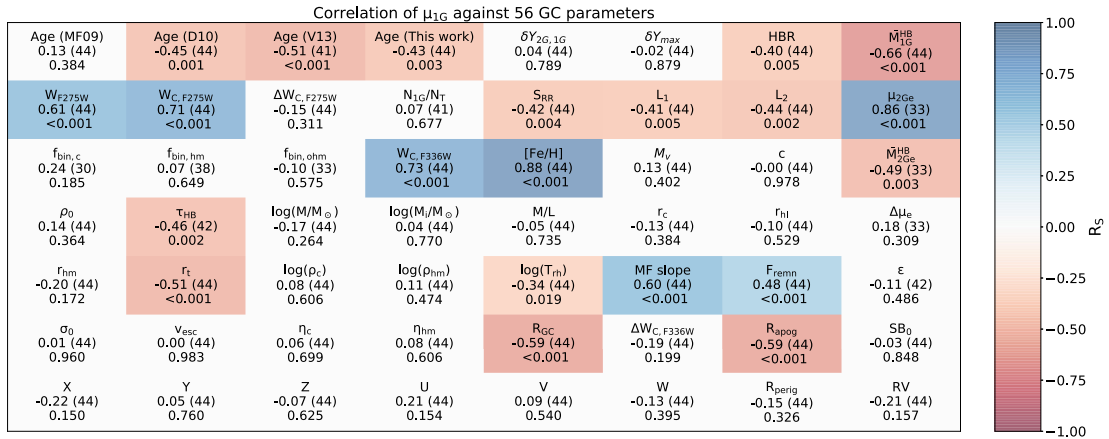
Figure B1. Correlation of μ_{1G} against 56 GC parameters. Each cells in the figure represents a parameter. The first row reports the name of parameter (see Section B and Table B1). The second row reports the value of the Spearman rank coefficient (R_s) and the number of degrees of freedom. The last row in the cells reports the *p*-value for the test. Each cell is colour coded according to the value of R_s. No colour has been assigned to non-significant correlations ($p > 0.05$).

of 2Ge stars exhibit strong anticorrelations with $\Delta W_{C,F275W}$, W_{F275W}, and $W_{C,F275W}$ ($R_S \lesssim -0.7$). Additional correlations and anticorrelations involve $\delta Y_{2G,1G}$, δY_{max}, $f_{bin,hm}$, $W_{C,F336W}$, M_V, present-day mass and the initial mass of the host cluster, ρ_{hm}, σ_0, SB_0, and v_{esc}. Noticeable, these quantities correlate or anticorrelate with each other (e.g. Milone et al. [2017](#), [2020](#); Lagioia et al. [2019](#)). Similar conclusion can be extended to $\Delta \mu_e$ (Fig. B4).

Correlation of μ_{2Ge} against 56 GC parameters

Age (MF09) -0.11 (33) 0.548	Age (D10) -0.24 (33) 0.160	Age (V13) -0.13 (33) 0.484	Age (This work) -0.17 (33) 0.324	$\delta Y_{2G,1G}$ 0.23 (33) 0.178	δY_{max} 0.21 (33) 0.224	HBR 0.10 (33) 0.550	μ_{1G} 0.86 (33) <0.001
W_{F275W} 0.59 (33) <0.001	$W_{C,F275W}$ 0.77 (33) <0.001	$\Delta W_{C,F275W}$ 0.41 (33) 0.014	N_{1G}/N_T -0.24 (32) 0.164	S_{RR} -0.23 (33) 0.174	L_1 0.07 (33) 0.671	L_2 0.19 (33) 0.262	$\bar{M}^{HB}_{1G}$ -0.70 (33) <0.001
$f_{bin,c}$ -0.22 (22) 0.301	$f_{bin,hm}$ -0.33 (28) 0.075	$f_{bin,ohm}$ -0.41 (26) 0.030	$W_{C,F336W}$ 0.71 (33) <0.001	[Fe/H] 0.70 (33) <0.001	M_v -0.21 (33) 0.224	c 0.17 (33) 0.329	$\bar{M}^{HB}_{2Ge}$ -0.81 (33) <0.001
ρ_0 0.36 (33) 0.034	τ_{HB} 0.16 (32) 0.359	$\log(M/M_\odot)$ 0.21 (33) 0.220	$\log(M_i/M_\odot)$ 0.42 (33) 0.011	M/L 0.10 (33) 0.568	r_c -0.29 (33) 0.094	r_{hl} -0.37 (33) 0.027	$\Delta\mu_e$ 0.60 (33) <0.001
r_{hm} -0.49 (33) 0.003	r_t -0.26 (33) 0.136	$\log(\rho_c)$ 0.33 (33) 0.051	$\log(\rho_{hm})$ 0.48 (33) 0.004	$\log(T_{rh})$ -0.40 (33) 0.016	MF slope 0.60 (33) <0.001	F_{remn} 0.38 (33) 0.026	ϵ -0.25 (31) 0.154
σ_0 0.38 (33) 0.024	v_{esc} 0.37 (33) 0.028	η_c -0.03 (33) 0.846	η_{hm} -0.04 (33) 0.810	R_{GC} -0.51 (33) 0.002	$\Delta W_{C,F336W}$ 0.21 (33) 0.220	R_{apog} -0.61 (33) <0.001	SB_0 -0.34 (33) 0.049
X -0.18 (33) 0.301	Y 0.06 (33) 0.738	Z -0.01 (33) 0.936	U 0.02 (33) 0.921	V 0.00 (33) 0.994	W -0.22 (33) 0.195	R_{perig} -0.38 (33) 0.023	RV -0.11 (33) 0.519

Figure B2. As Fig. B1 but for μ_{2Ge}.

Correlation of $\bar{M}^{HB}_{1G}$ against 56 GC parameters

Age (MF09) -0.09 (44) 0.550	Age (D10) -0.01 (44) 0.886	Age (V13) -0.02 (41) 0.973	Age (This work) -0.01 (44) 0.954	$\delta Y_{2G,1G}$ 0.06 (44) 0.671	δY_{max} 0.17 (44) 0.262	HBR -0.32 (44) 0.028	μ_{1G} -0.66 (44) <0.001
W_{F275W} -0.12 (44) 0.446	$W_{C,F275W}$ -0.28 (44) 0.057	$\Delta W_{C,F275W}$ 0.03 (44) 0.865	N_{1G}/N_T 0.02 (41) 0.874	S_{RR} 0.35 (44) 0.017	L_1 -0.32 (44) 0.032	L_2 0.30 (44) 0.045	μ_{2Ge} -0.70 (33) <0.001
$f_{bin,c}$ 0.05 (30) 0.778	$f_{bin,hm}$ 0.11 (38) 0.494	$f_{bin,ohm}$ 0.18 (33) 0.305	$W_{C,F336W}$ -0.27 (44) 0.069	[Fe/H] -0.37 (44) 0.012	M_v -0.23 (44) 0.131	c 0.00 (44) 0.993	$\bar{M}^{HB}_{2Ge}$ 0.45 (33) 0.006
ρ_0 -0.04 (44) 0.778	τ_{HB} -0.17 (42) 0.282	$\log(M/M_\odot)$ 0.21 (44) 0.160	$\log(M_i/M_\odot)$ 0.01 (44) 0.941	M/L -0.10 (44) 0.511	r_c 0.17 (44) 0.263	r_{hl} 0.11 (44) 0.477	$\Delta\mu_e$ -0.09 (33) 0.617
r_{hm} 0.24 (44) 0.114	r_t 0.53 (44) <0.001	$\log(\rho_c)$ -0.13 (44) 0.404	$\log(\rho_{hm})$ -0.02 (44) 0.891	$\log(T_{rh})$ 0.42 (44) 0.004	MF slope -0.50 (44) <0.001	F_{remn} -0.42 (44) 0.004	ϵ 0.18 (42) 0.242
σ_0 0.05 (44) 0.738	v_{esc} 0.06 (44) 0.685	η_c -0.05 (44) 0.727	η_{hm} 0.22 (44) 0.139	R_{GC} 0.53 (44) <0.001	$\Delta W_{C,F336W}$ 0.19 (44) 0.216	R_{apog} 0.57 (44) <0.001	SB_0 -0.05 (44) 0.766
X 0.10 (44) 0.516	Y -0.20 (44) 0.181	Z -0.03 (44) 0.862	U -0.05 (44) 0.734	V -0.06 (44) 0.702	W 0.17 (44) 0.266	R_{perig} 0.27 (44) 0.068	RV 0.10 (44) 0.512

Figure B3. As Fig. B1 but for $\bar{M}^{HB}_{1G}$.

Correlation of $\bar{M}^{HB}_{2Ge}$ against 56 GC parameters

Age (MF09) 0.14 (33) 0.418	Age (D10) 0.08 (33) 0.648	Age (V13) 0.07 (30) 0.722	Age (This work) -0.02 (33) 0.915	$\delta Y_{2G,1G}$ -0.54 (33) <0.001	δY_{max} -0.62 (33) <0.001	HBR -0.21 (33) 0.230	μ_{1G} -0.49 (33) 0.003
W_{F275W} -0.72 (33) <0.001	$W_{C,F275W}$ -0.70 (33) <0.001	$\Delta W_{C,F275W}$ -0.74 (33) <0.001	N_{1G}/N_T 0.44 (32) 0.008	S_{RR} 0.38 (33) 0.025	L_1 -0.13 (33) 0.449	L_2 -0.26 (33) 0.136	$\bar{M}^{HB}_{1G}$ 0.45 (33) 0.006
$f_{bin,c}$ 0.47 (22) 0.022	$f_{bin,hm}$ 0.55 (28) 0.002	$f_{bin,ohm}$ 0.40 (26) 0.036	$W_{C,F336W}$ -0.59 (33) <0.001	[Fe/H] -0.38 (33) 0.026	M_v 0.53 (33) <0.001	c -0.25 (33) 0.148	μ_{2Ge} -0.81 (33) <0.001
ρ_0 -0.49 (33) 0.003	τ_{HB} -0.45 (32) 0.007	$\log(M/M_\odot)$ -0.56 (33) <0.001	$\log(M_i/M_\odot)$ -0.65 (33) <0.001	M/L 0.05 (33) 0.781	r_c 0.35 (33) 0.041	r_{hl} 0.49 (33) 0.003	$\Delta\mu_e$ -0.82 (33) <0.001
r_{hm} 0.55 (33) <0.001	r_t -0.02 (33) 0.896	$\log(\rho_c)$ -0.44 (33) 0.008	$\log(\rho_{hm})$ -0.68 (33) <0.001	$\log(T_{rh})$ 0.30 (33) 0.080	MF slope -0.42 (33) 0.013	F_{remn} -0.11 (33) 0.522	ϵ 0.09 (31) 0.611
σ_0 -0.66 (33) <0.001	v_{esc} -0.64 (33) <0.001	η_c 0.04 (33) 0.816	η_{hm} 0.02 (33) 0.925	R_{GC} 0.36 (33) 0.036	$\Delta W_{C,F336W}$ -0.49 (33) 0.003	R_{apog} 0.48 (33) 0.003	SB_0 0.54 (33) <0.001
X 0.04 (33) 0.820	Y -0.05 (33) 0.756	Z 0.01 (33) 0.955	U 0.01 (33) 0.972	V -0.08 (33) 0.636	W 0.24 (33) 0.166	R_{perig} 0.42 (33) 0.013	RV 0.13 (33) 0.461

Figure B4. As Fig. B1 but for $\bar{M}^{HB}_{2Ge}$.

Correlation of Δμ_e against 56 GC parameters

Age (MF09) -0.11 (33) 0.526	Age (D10) -0.11 (33) 0.523	Age (V13) -0.02 (30) 0.898	Age (This work) 0.12 (33) 0.480	$\delta Y_{2G,1G}$ 0.46 (33) 0.006	δY_{max} 0.61 (33) <0.001	HBR -0.01 (33) 0.938	μ_{1G} 0.18 (33) 0.309
W_{F275W} 0.67 (33) <0.001	$W_{C,F275W}$ 0.58 (33) <0.001	$\Delta W_{C,F275W}$ 0.76 (33) <0.001	N_{1G}/N_T -0.51 (32) 0.002	S_{RR} -0.08 (33) 0.667	L_1 -0.07 (33) 0.696	L_2 0.46 (33) 0.005	$\bar{M}_{1G}^{HB}$ -0.09 (33) 0.617
$f_{bin,c}$ -0.41 (22) 0.049	$f_{bin,hm}$ -0.56 (28) 0.001	$f_{bin,ohm}$ -0.49 (26) 0.009	$W_{C,F336W}$ 0.49 (33) 0.003	[Fe/H] 0.21 (33) 0.228	M_V -0.62 (33) <0.001	c 0.21 (33) 0.219	μ_{2Ge} 0.60 (33) <0.001
ρ_0 0.49 (33) 0.003	τ_{HB} 0.33 (32) 0.057	$\log(M/M_\odot)$ 0.61 (33) <0.001	$\log(M_i/M_\odot)$ 0.73 (33) <0.001	M/L -0.10 (33) 0.573	r_c -0.32 (33) 0.057	r_{hl} -0.53 (33) 0.001	$\bar{M}_{2Ge}^{HB}$ -0.82 (33) <0.001
r_{hm} -0.54 (33) <0.001	r_t 0.20 (33) 0.261	$\log(\rho_c)$ 0.43 (33) 0.009	$\log(\rho_{hm})$ 0.74 (33) <0.001	$\log(T_{rh})$ -0.22 (33) 0.213	MF slope 0.31 (33) 0.069	F_{remn} 0.05 (33) 0.771	ε -0.02 (31) 0.927
σ_0 0.69 (33) <0.001	v_{esc} 0.68 (33) <0.001	η_c -0.09 (33) 0.595	η_{hm} -0.07 (33) 0.673	R_{GC} -0.16 (33) 0.346	$\Delta W_{C,F336W}$ 0.62 (33) <0.001	R_{apog} -0.26 (33) 0.125	SB_0 -0.59 (33) <0.001
X 0.05 (33) 0.766	Y -0.00 (33) 0.992	Z -0.01 (33) 0.976	U 0.03 (33) 0.843	V 0.00 (33) 0.985	W -0.11 (33) 0.527	R_{perig} -0.42 (33) 0.012	RV -0.10 (33) 0.584

Figure B5. As Fig. B1 but for $\Delta\mu_e$.

APPENDIX C: THE AGE–METALLICITY RELATION AND THE IMPACT OF AGE ON THE HB MORPHOLOGY

In the following, we further investigate the impact of age and metallicity on the HB morphology. A visual inspection at the left-hand panel of Fig. C1 reveals that, based on the ages derived in this paper, the metal-poor GCs are, on average, older than the metal-rich ones. To quantify age variation as a function of metallicity, we defined five intervals of iron abundance, ranging from [Fe/H] = −2.5 to solar in bins of 0.5 dex and estimate the average age of GC in each bin (red squares in the left-hand panel of Fig. C1). Clearly, the average age decreases towards higher metallicity with clusters having [Fe/H] > −1.5 being, on average, ∼0.75 Gyr younger of their metal-poor counterparts.

The age–metallicity relation derived in this work is similar to the one by Dotter et al. (2010) for the same GCs. Moreover, we find that GCs with large Galactocentric distances ($R_{GC} > 8$ kpc) are older than those with $R_{GC} < 8$ kpc, thus confirming previous conclusion that the age–metallicity relation is composed of two branches (e.g. Forbes & Bridges 2010; Dotter, Sarajedini & Anderson 2011; Kruijssen et al. 2019). This result is quite expected. Indeed, , as shown in the upper-right panel of Fig. C1, when we compare our ages with those by Dotter et al. (2010) we find a good agreement (at 1σ level). On the contrary, our ages are systematically older by ∼0.75 Gyr than those provided by VandenBerg et al. (2013) and the age difference, which is significant at more than 3σ, increases with metallicity.

Fig. C1 reveals that M3- and M13-like GCs have different average ages (12.5 ± 0.1 and 13.0 ± 0.1 Gyr, respectively). To further
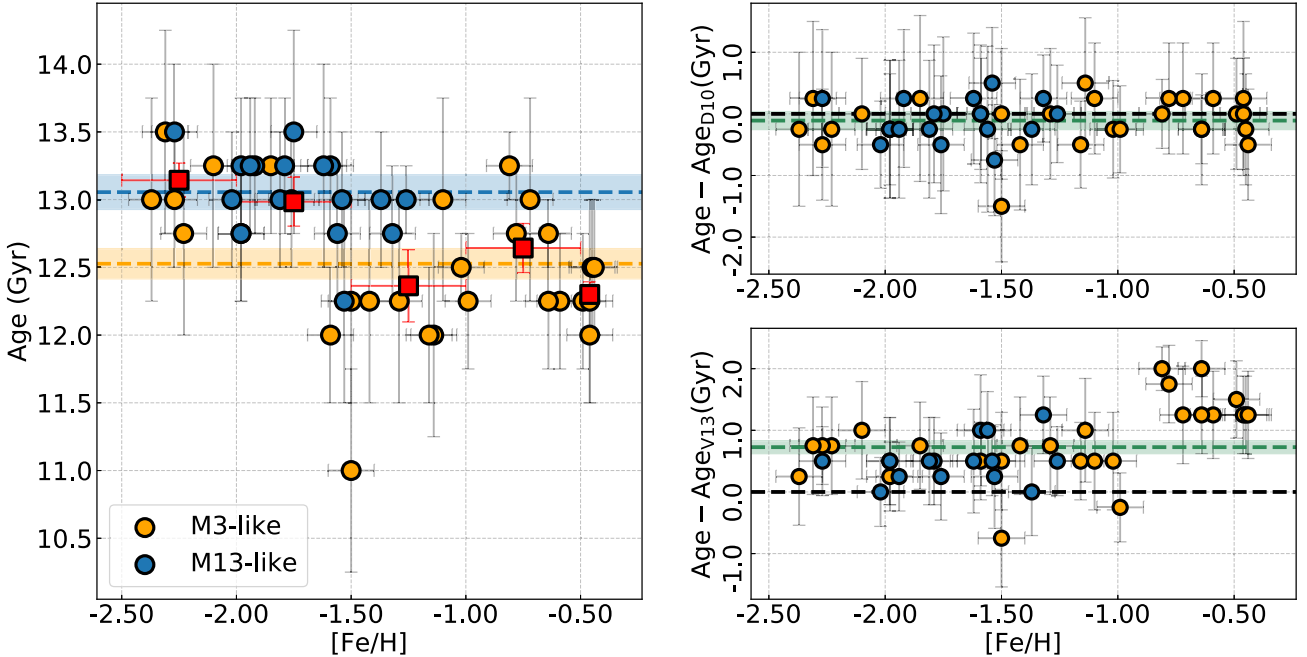

Figure C1. *Left-hand panel:* Age as function of the [Fe/H] value for the GC in our sample. M3- and M13-like GCs are represented as orange and blue dots, respectively. The red squares represent the average age values of different [Fe/H] intervals (see text) while the two dashed lines are the average age of the M3- and M13-like clusters, together with their 1σ intervals. *Right-hand panels:* Comparison of the results of this work with the ones from Dotter et al. (2010, D10, top) and VandenBerg et al. (2013, V13, bottom). The green dashed lines represent the average age difference between two sets, together with their 1σ intervals.
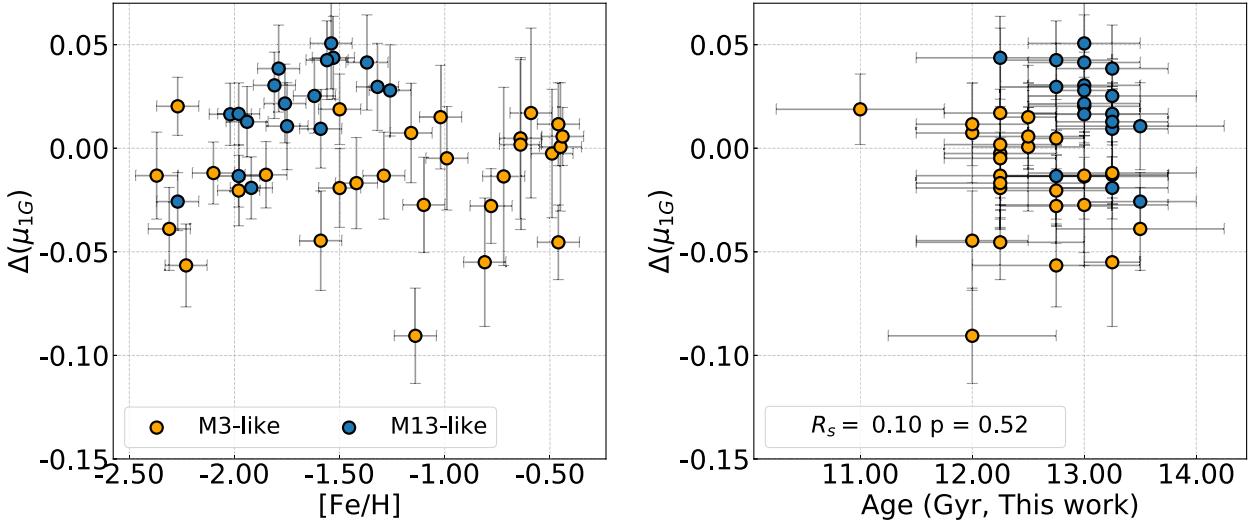
Figure C2. Residuals relative to equation (1) of the main text ($\Delta(\mu_{1G})$) as function of [Fe/H] (left-hand panel) and age (right-hand panel).

investigate the relation between age and mass-loss, we show in the right-hand panel of Fig. C2 the mass-loss residuals to equation (1) [$\Delta(\mu_{1G})$] against [Fe/H] and age. Although there is no significant correlation between these two quantities ($R_S = 0.1$), possibly as a consequence of their relatively-large error bars, we conclude that M13-like GCs are older and lose more mass than M3-like GCs and such differences are significant at more than 4σ level. We verify that similar conclusions are inferred by using the ages by Dotter et al. (2010, 2011), VandenBerg et al. (2013), and Marín-Franch et al. (2009).

However, the evidence that M3- and M13-like GCs exhibit different HB shapes (Milone et al. 2014, see their fig. 2) and have different mass-losses does not indicate that age is responsible for the HB morphology. The reason to exclude age as a second parameter of the HB morphology, is that the simulated HBs used to infer the mass-loss properly take into account cluster ages. This fact is clearly illustrated in Fig. 6, where we show how each value of M_{1G}^{Tip} that we inferred in this work is tailored for a specific cluster and is derived by using the corresponding age. Moreover, the comparison between observed and simulated HBs represented in Fig. 6 reveals that difference in M_{1G}^{Tip} induced by an age difference of 0.5 Gyr is ~ 0.01 M$_\odot$. Such a small amount of mass is not enough to compensate the differences in the 1G HB mass observed between the M3- and M13-like GCs, even if our simulations had not taken age into account.

We conclude that age does not play a major role in determining the HB morphology of Galactic GCs, thus challenging the conclusion by several papers, where age is considered a second parameter of the HB morphology in GCs (e.g. Sandage & Wildey 1967b; Dotter et al. 2010; Gratton et al. 2010; VandenBerg et al. 2013; Milone et al. 2014). Anyway, the small age difference found between the M3- and the M13-like GCs leaves some residual space to argue that it may cause (through the small difference in evolving mass) a second-order effect on the mass lost by their RGB stars, linked to the complex influence of pulsation and magneto-acoustic processes, still largely unknown, on mass-loss (e.g. McDonald & van Loon 2007).

APPENDIX D: STANDARD HELIUM FLASH MODELS

Standard models and evolutionary effects do not predict the increased mass-loss needed to describe the location of the 2Ge HB stars in the CMD. To show this, we compare the evolution through the helium flash of a series of stellar tracks with different initial helium in Fig. D1.

The models shown here have [Fe/H] = –2.44 and –1.44, and are obtained with $\eta_R = 0.3$. All tracks reach the corresponding RGB tip in 12.0 Gyr. Since each model refers to different helium abundance, we have smaller masses for higher helium. In particular for [Fe/H] = –2.44 with Y = 0.25, 0.28, 0.35, 0.40, we have M = 0.806, 0.765, 0.674, 0.613, M$_\odot$, respectively; for [Fe/H] = –1.44 and the same Y's, we have M = 0.828, 0.786, 0.692, 0.628 M$_\odot$. The considerations we make in this section are valid for our entire data base.

We plot in the left-hand panel of Fig. D1 the fraction of the model luminosity coming from the 3α reaction chains [$\log(L_{3\alpha}/L_\star)$], involved in the helium flash, as a function of the total luminosity of the star [$\log(L_\star/L_\odot)$], a proxy of the evolutionary stage. The right-hand panel of Fig. D1, on the other hand, shows the total mass lost ($\Delta M/$M$_\odot$) as function of the total luminosity for the models.

From the figure, we get a crucial clue: the helium flash starts ($\log L_{3\alpha}/L_\star > -2.5$) at progressively lower luminosity for increasing Y. This implies that, within a single family of models describing a Type I cluster, the mass-loss rate cannot vary too much without any additional inputs. If we consider that the models complete their evolution at the same time, and that helium-rich models have slightly shorter RGB phases, the total mass lost should be decreasing as Y increases (note that the increase in the mass lost between the two families of models is due to their different metallicity and not their helium abundance, see Fig. 16). These considerations strengthen the need to include additional physical inputs to the standard models to obtain results in agreement with the observations.

Again, we notice that an independent alternative explanation of the data might be possible. The physics of mass-loss in the framework of the combination of pulsation and magneto-acoustic processes (see e.g. McDonald & van Loon 2007), at the time of this writing, is not modelled in 1D stellar evolution codes, so there is some space left to argue that the enhanced helium abundance of the 2Ge stars might concur to increase their surface activity in the RGB phase, ending in an increase in the instantaneous mass-loss rate, so that the 2Ge stars naturally lose more mass during their evolution. The correlation with helium shown in Fig. 12 would then be the natural outcome of such interactions.
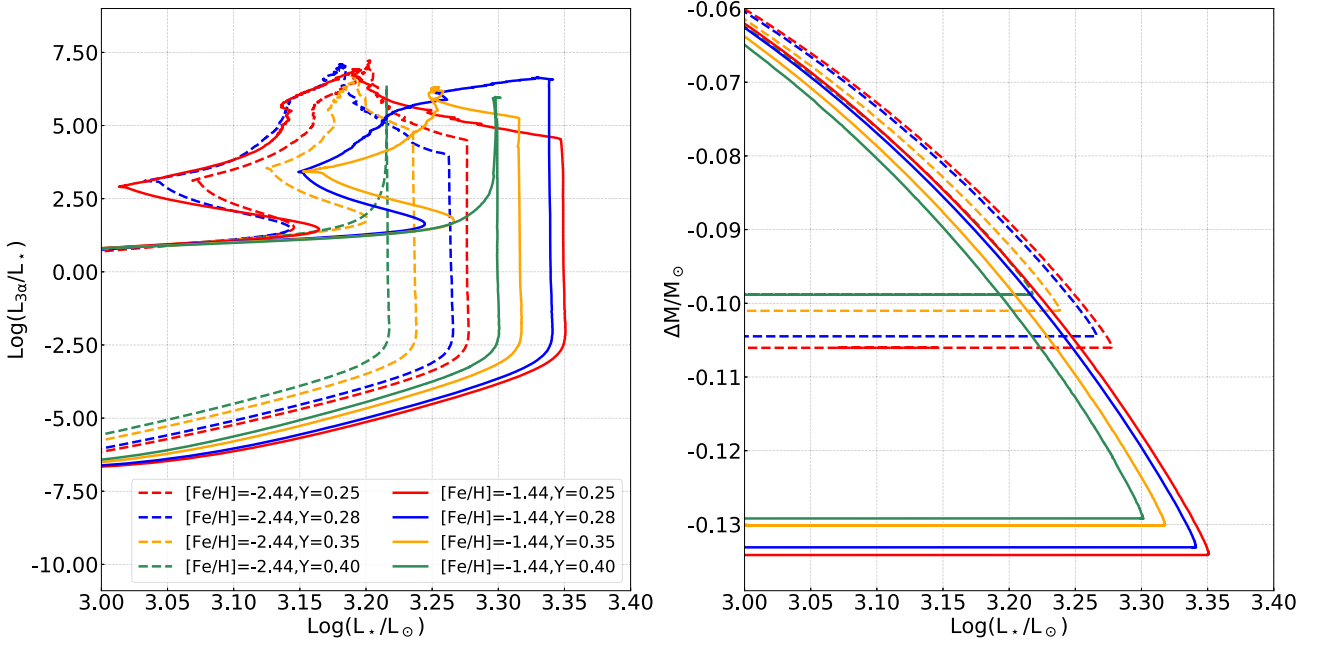
Figure D1. *Left-hand panel:* Fraction of the stellar luminosity coming from 3α reactions, tracer of the helium flash process, as function of the total luminosity, tracer of the evolutionary stage. *Right-hand panel:* Total mass lost ($\Delta M/\mathrm{M_\odot}$) by the models in the left-hand panel as function of luminosity.

This paper has been typeset from a TeX/LaTeX file prepared by the author.